

AN EXPERIMENTAL STUDY OF FLOW SEPARATION OVER A FLAT PLATE WITH 2D  
TRANSVERSE GROOVES

by

EMILY MICHELLE JONES

AMY W. LANG, COMMITTEE CHAIR  
J. PAUL HUBNER  
AJAY K. AGRAWAL

A THESIS

Submitted in partial fulfillment of the requirements  
for the degree of Master of Science  
in the Department of Aerospace Engineering and Mechanics  
in the Graduate School of the  
University of Alabama

TUSCALOOSA, ALABAMA

2013

Copyright Emily Michelle Jones 2013  
ALL RIGHTS RESERVED

## ABSTRACT

Nature has long been an inspiration for research in engineering. In particular, the biological surfaces of aquatic swimmers have been studied for their potential as drag reducing surfaces. The hydrodynamic benefit of riblets, or grooves embedded parallel to the flow, which appear on many aquatic biological surfaces, have been well documented and implemented in practical engineering applications. However the skin of dolphins is embedded with grooves that run perpendicular to the flow of water over their bodies. It is theorized that the transverse grooves present on dolphin skin trap vortices between them, creating a partial slip condition over the surface and inducing turbulence augmentation in the boundary layer, thus controlling boundary layer separation over the dolphin's skin. Similarly, sharks are covered with scales that are flexible at the base and capable of bristling, forming grooves running transverse to the flow. It is theorized that the scales bristle when encountering a reversing flow, thereby trapping vortices between the scales and, similarly, delaying boundary layer separation. In an attempt to test this hypothesis and study these affects, a spinning cylinder was used in a water tunnel to induce separation over a flat plate with 2 mm, rectangular transverse grooves and sinusoidal grooves of similar scaling. The results were compared to tripped, turbulent boundary layer separation occurring over a flat plate without grooves using time-resolved particle image velocimetry. The strength of the adverse pressure gradient was varied, and the observed delay in flow separation and other affects upon the boundary layer are discussed.

## LIST OF SYMBOLS

$\alpha$	=	angle of the trailing edge with relation to the flat plate
$\omega$	=	angular velocity of the cylinder (rpm)
$\delta$	=	boundary layer thickness
$u$	=	the component of the velocity that runs parallel to the plate, positive downstream
$v$	=	the component of the velocity normal to the plate, positive away from the plate
$\nabla$	=	the del operator
$\rho$	=	density
$D$	=	diameter of cylinder
$x$	=	the direction parallel to the plate, positive downstream
$y$	=	the direction normal to the plate, positive away from the plate
$\mu$	=	dynamic viscosity
$u'$	=	fluctuation in the u component of the velocity about the mean
$v'$	=	fluctuation in the v component of the velocity about the mean
$U_\infty$	=	free stream velocity
$x$	=	horizontal distance from leading edge to cylinder center
$L$	=	length of the plate
$\theta$	=	momentum deficit
$p$	=	period of the groove geometry
$Re$	=	Reynolds's number

- $\tau$  = Reynolds stress
- $VR$  = non-dimensionalized strength of the pressure gradient
- $\vec{v}$  = velocity vector
- $y$  = vertical distance from flat plate to cylinder center
- $\vec{\xi}$  = vorticity

## ACKNOWLEDGEMENTS

I would like to thank my project mentor and committee chair, Dr. Amy Lang, for the opportunity to participate in this research and her invaluable guidance throughout this research project. I would also like to thank Dr. Paul Hubner and Dr. Ajay Agrawal for taking the time to serve on my thesis committee. I am very thankful for the assistance in the water tunnel lab with my project, both in helping conceptually and with conducting experiments, of my lab mates: Farhana Afroz, Jennifer Wheelus, and Michael Bradshaw. I would like to acknowledge my appreciation for the work of the engineering machine shop in the construction of the models for my experiments. I also greatly appreciate the financial support of the University of Alabama Graduate Council and the National Science Foundation during the course of my graduate education.

## CONTENTS

ABSTRACT.....	ii
LIST OF SYMBOLS.....	iii
ACKNOWLEDGEMENTS.....	v
LIST OF TABLES.....	viii
LIST OF FIGURES.....	xi
1. INTRODUCTION.....	1
1.1 BOUNDARY LAYER SEPARATION CONTROL.....	1
1.2 SHARK AND DOLPHIN SKIN SEPARATION CONTROL TECHNIQUES .....	2
1.3 OBJECTIVE.....	6
1.4 DEFINITIONS AND EQUATIONS.....	7
2. REVIEW OF LITERATURE.....	10
2.1 TURBULENT BOUNDARY LAYERS.....	10
2.2 TURBULENT BOUNDARY LAYER SEPARATION.....	11
2.3 GENERATION OF AN ADVERSE PRESSURE GRADIENT.....	13
2.4 METHODS OF SEPARATION CONTROL.....	14
2.5 DOLPHIN AND SHARK SKIN.....	15
3. EXPERIMENTAL SETUP.....	18

1.1 EXPERIMENTAL FACILITY.....	18
1.2 EXPERIMENTAL MODEL.....	19
1.3 DPIV SYSTEM.....	21
1.4 EXPERIMENTAL PROCEDURE.....	23
2. RESULTS AND DISCUSSION.....	26
2.1 MEAN VELOCITY FIELD CONTOUR COMPARISON.....	26
2.2 MEAN VELOCITY PROFILE COMPARISON.....	28
2.3 PARTIAL SLIP ANALYSIS AND COMPARISON.....	32
2.4 BACKFLOW COEFFICIENT CONTOURS.....	35
2.5 TRANSIENT BOUNDARY LAYER SEPARATION OVER THE FLAT PLATE..	37
2.6 MEAN REYNOLDS STRESS FIELD.....	38
2.7 MEAN REYNOLDS STRESS PROFILE COMPARISON.....	40
2.8 PEAK REYNOLDS STRESS COMPARISON.....	43
2.9 MEAN V VELOCITY FIELD COMPARISON.....	47
2.10 VORITICITY FIELD COMPARISON.....	49
2.11 TURBULENCE INTENSITY FIELD COMPARISON.....	51
3. CONCLUSIONS.....	53
3.1 MECHANISMS OF BOUNDARY LAYER SEPARATION CONTROL.....	53
3.2 FUTURE WORK.....	55
REFERENCES.....	56
APPENDIX A- ADDITIONAL DATA.....	58
APPENDIX B – UNCERTAINTY ANALYSIS.....	63

## LIST OF TABLES

1. Slip velocity comparison.....	32
2. Percent average slip velocities.....	32

## LIST OF FIGURES

1. Comparison of traditional and current views of TBL separation (Simpson 1996).....	2
2. Bristled v. non-bristled Mako shark scales.....	3
3. Theorized progression of passive separation control of Mako shark scales.....	4
4. Groove distribution over a dolphin's body.....	5
5. Diagram of rectangular v. sinusoidal grooved models.....	6
6. Potential flow pressure distribution over the flat plate.....	7
7. Fluctuating backflow region example images (Angele et al).....	12
8. Dye visualization of separation due to spinning cylinder.....	13
9. The University of Alabama water tunnel facility.....	18
10. Image of the flat plate model.....	20
11. Model of the experimental setup.....	20
12. Diagram of the model sections.....	21
13. Diagram of data capture setup.....	22
14. Images of camera and laser.....	23
15. Example final processed grid.....	25
16. Comparison of U velocity averages.....	27
17. Velocity profile comparison at zero pressure gradient.....	28
18. Comparison of velocity profiles under adverse pressure gradient.....	31

19. Comparison plot of slip velocities.....	33
20. Comparison of backflow coefficient over the flat plate model.....	34
21. Comparison of backflow coefficient over the grooved plate models.....	35
22. Series of U velocity averages demonstrating turbulent separation.....	36
23. Comparison of Reynolds stresses under 1 <sup>st</sup> pressure gradient.....	37
24. Comparison of Reynolds stress profiles under zero pressure gradient.....	39
25. Comparison of Reynolds stress profiles under 1 <sup>st</sup> pressure gradient.....	41
26. Comparison of Reynolds stress profiles under 2 <sup>nd</sup> pressure gradient.....	42
27. Peak Reynolds stress values compared at zero pressure gradient.....	43
28. Comparison of peak Reynolds stress values.....	44
29. Comparison of height of peak Reynolds stress values.....	45
30. Comparison of V velocity contours at 1 <sup>st</sup> pressure gradient.....	47
31. Comparison of V velocity contours at 2 <sup>nd</sup> pressure gradient.....	48
32. Comparison of vorticity field contours over the grooved plates.....	50
33. Comparison of turbulence intensity fields.....	51

## 1. INTRODUCTION

### 1.1 BOUNDARY LAYER SEPARATION

Boundary layer separation occurs on a surface when the flow over that surface encounters an adverse pressure gradient of sufficient strength to stop and reverse the flow of the fluid within the boundary layer. Such separation causes an increase in pressure drag, and decreases the effectiveness of control surfaces within the region of separated flow. A delay in the onset of boundary layer separation will delay the onset of stall on an airfoil, increase the effectiveness of a propeller or control surfaces, and reduce pressure drag, thereby increasing the fuel efficiency of automobiles or aircraft. For these reasons, much research attention is devoted to reducing or delaying boundary layer separation.

In the case of initially laminar 2D flow, the boundary layer separates at the point in the flow where the shear stress on the wall equals zero and transitions to turbulence. It then may reattach to the surface and creates a stationary bubble of separated flow. Due to the complexity of turbulent flow, zero wall shear stress does not occur at one stationary point, therefore separation occurs intermittently over a surface, and a specific point of separation is difficult to define. For this reason, Simpson [15] defines several points of separation in a turbulent boundary layer, relating each to a different percentage of total flow that is reversed: incipient detachment, intermittent transitory detachment, and transitory detachment. These points are illustrated in Figure 1.1. Incipient detachment is defined as the point at which the flow is reversed 1% of the time, while intermittent transitory detachment occurs when the flow reverses 20% of the time.

Transitory detachment, also the point at which the shear stress on the wall averages to zero over time, is the point at which the flow at the surface is reversed 50% of the time. These stationary locations can be used to quantify the process of separation in a turbulent boundary layer.

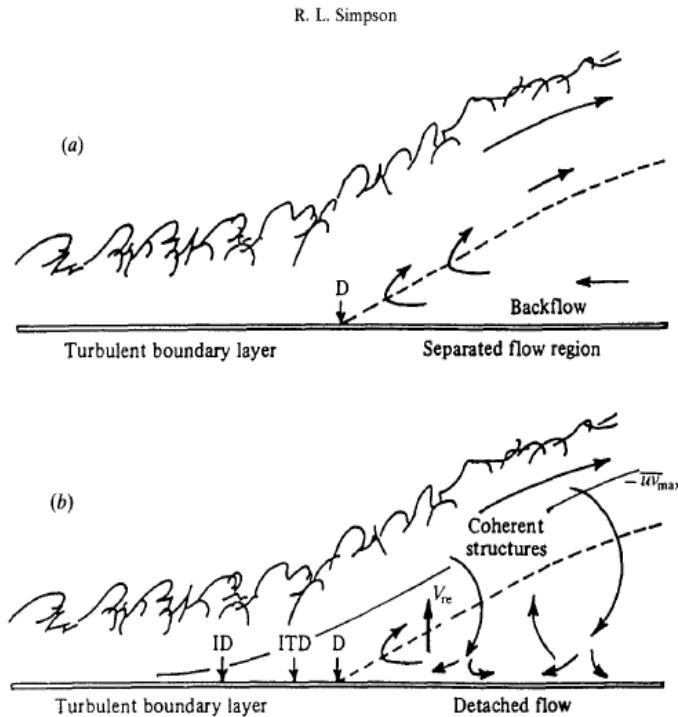


Figure 1.1 (a) Traditional view of turbulent boundary layer separation. (b) Currently accepted view, showing points of quantitative definitions of reversed flow percentages [15].

## 1.2 SHARK SKIN AND DOLPHIN SKIN SEPERATION CONTROL TECHNIQUES

Bio-inspired technology research is a topic of special interest in the field of fluid mechanics. In nature, the wings of birds and insects or the skin of fish are typically patterned with feathers or scales to protect the animal and keep it healthy. However, there may also be an aerodynamic benefit to such surface patterning.

The Shortfin Mako shark (*Isurus oxyrinchus*) is one of nature's fastest swimmers. In the open ocean it has been observed to achieve speeds as high as 20 m/s and make rapid direction

changes and turns. It is theorized by Lang [7] that the scales covering the Mako's body are a means by which the shark can passively delay boundary layer separation over its body. These scales, averaging 0.2 mm in size, are uniformly oriented from nose-to-tail and anchored to the shark's skin in such a way that they are able to pivot about their anchor. It is theorized that, under the influence of a tail to nose direction shearing force created by reversing flow, these scales may be caused to bristle, creating cavities between the bristled scales. Previous research at the University of Alabama has shown that such bristling does occur when the skin is acted upon by the shearing force of a tail-to-nose direction flow, and that the scales along the shark's body can bristle to an angle as high as 50 degrees. [8] It is interesting to note that the regions of the shark's skin where the highest bristling angles occur have been found to coincide with the regions where, due to the shark's body shape, the largest adverse pressure gradients would be expected to occur [7].

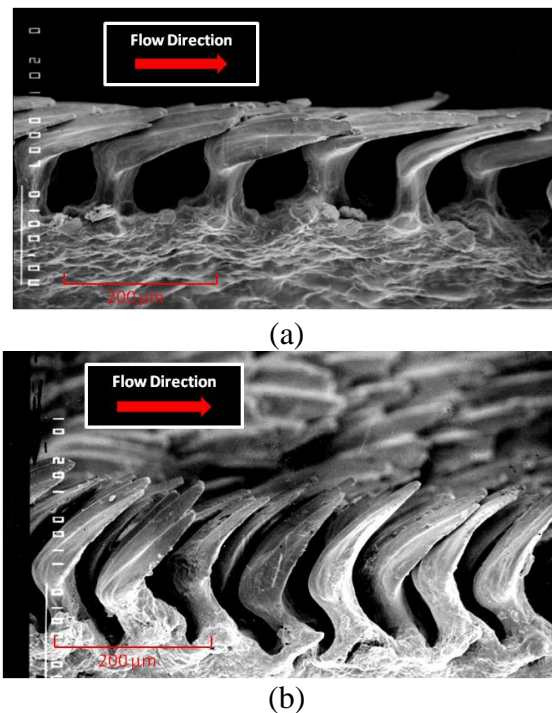


Figure 1.2 (a) SEM of non-bristled Mako scales. (b) SEM of bristled Mako scales and the formation of cavities between the scales [7]

It is theorized by Lang [7] that these cavities between the scales are able to catch the reversing flow and form vortices which act as roller bearings to the flow above the scales. These vortices cause a partial slip condition to occur in the region over the bristled scales, adding momentum to the flow close to the surface and, thereby, impeding the separation of the boundary layer.

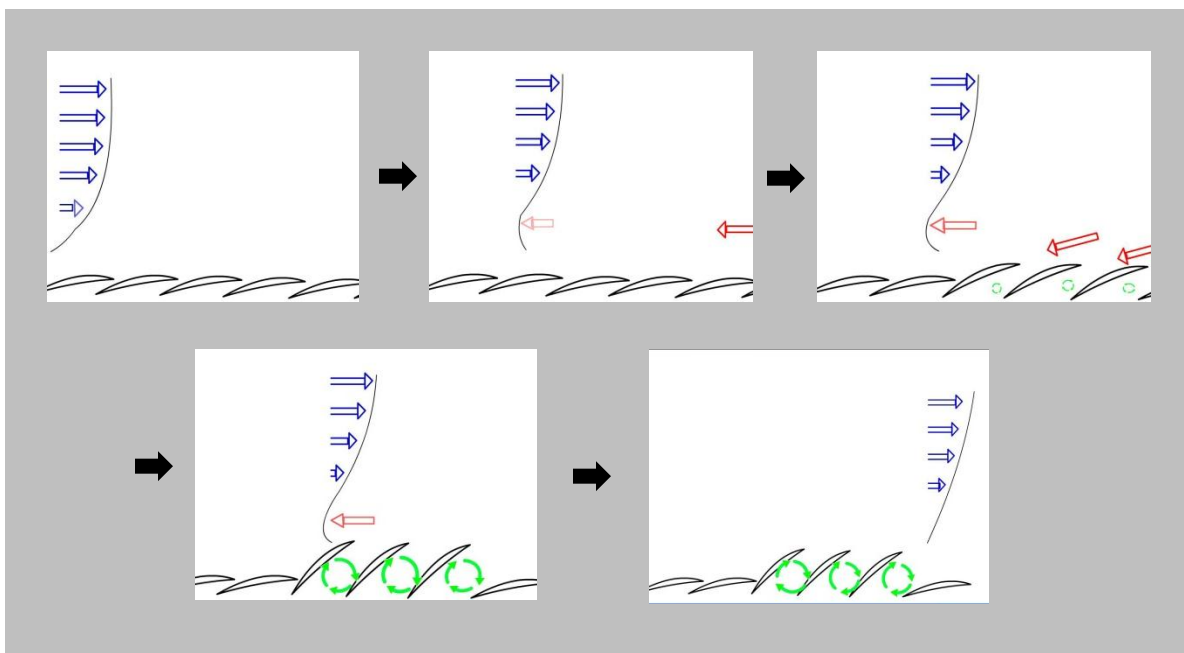


Figure 1.3: Theorized progression of passive separation control method employed by shark skin

Another biological surface of interest is that of dolphin skin. A dolphin's skin is grooved in the direction perpendicular to the flow over its body. These grooves are on average 0.04 cm in width, and 0.01 cm in depth.

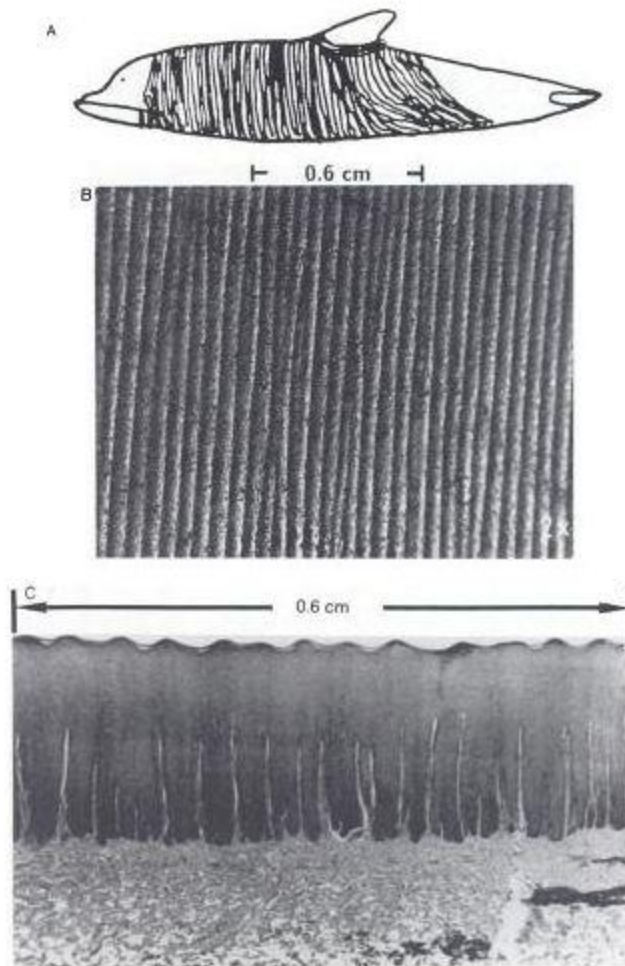


Figure 1.4 (a) Diagram of groove orientation on a dolphin's body (b) 2X Image of dolphin skin and (c) Image of a slice of the dolphin's skin [15]

It is theorized here that these grooves act in a way similar to the bristled shark scales in delaying the boundary layer separation over the dolphin's body. Embedded vortices form within the grooves reducing pressure drag over the dolphin's surface and acting to delay boundary layer separation in the presence of an adverse pressure gradient.

### 1.3 OBJECTIVE

The objective of this research was to test the theory that the presence of embedded vortices delays boundary layer separation and, if so, to examine the mechanisms by which such separation delay is achieved. The behavior of flow over a flat plate was compared to the flow over two 2D models: one with embedded rectangular grooves and one with embedded sinusoidal grooves. The rectangular grooves are 2 mm in width, 3 mm in depth, and separated by 1 mm partitions. The pseudo-sinusoidal grooves are 3 mm from peak to peak and 2 mm in depth. Cassel [4] stated that pressure perturbations in a turbulent boundary layer are proportional to the square root of the Reynolds number. Because these perturbations are the origin of separation, the width of the grooves was chosen to also be proportional to the square root of the Reynolds number. Choosing to make the grooves similar to the width of the cavities created between bristled shark scales, the inner width of the grooves is 2 mm.

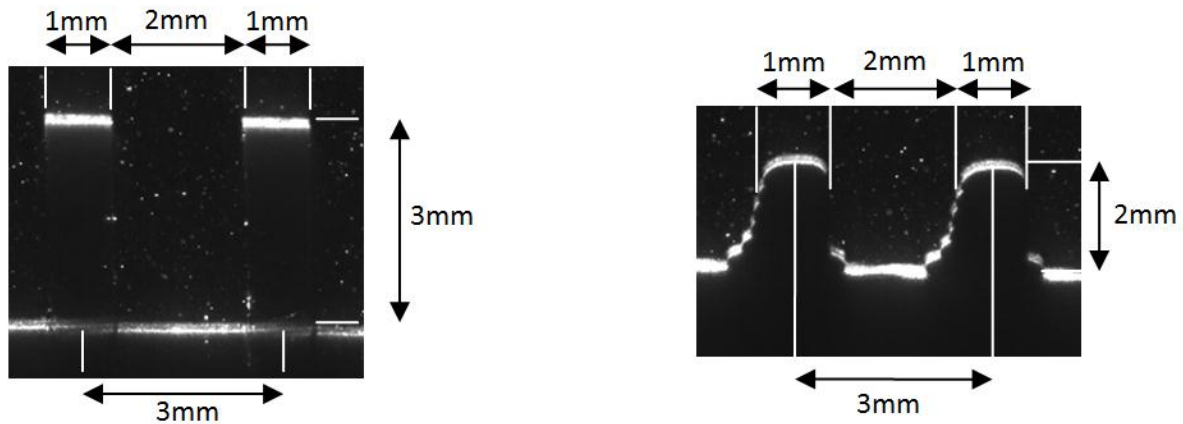


Figure 1.5 (a) Diagram of pseudo-sinusoidal model surface and (b) Diagram of rectangular grooved surface model

Through the use of a time resolved digital particle image velocimetry system, the flow over these three models was compared without a pressure gradient and, also, with two strengths of adverse pressure gradient, both sufficient to separate the flow over the flat plate. The adverse pressure gradient was achieved through the use of a spinning cylinder upstream of the observation point. This cylinder, with a diameter of 2.05 inches (5.2 cm), was spun at 200 and 260 RPM in order to produce the two adverse pressure gradients. When non-dimensionalized, using Equation 1, the adverse pressure gradients strengths are 2.12 and 2.76. The choice of these two strengths is somewhat arbitrary, but chosen as strengths at which reversed flow is observed. For the purposes of this discussion these pressure gradients strengths are simply referred to as the first and second pressure gradients. The equation is shown in Equation 1.

$$VR = \frac{2\pi}{60} * \frac{D^2 \omega}{4 * U_{\infty}} \quad (1)$$

For a given pressure gradient strength and ratio of cylinder diameter to height above the plate, the pressure gradient distribution can be estimated using potential flow theory [1]. The plots of the change in pressure distribution over the plate for the two pressure gradients used here are given in Figure 1.6. The red line represents the observation window of these experiments.

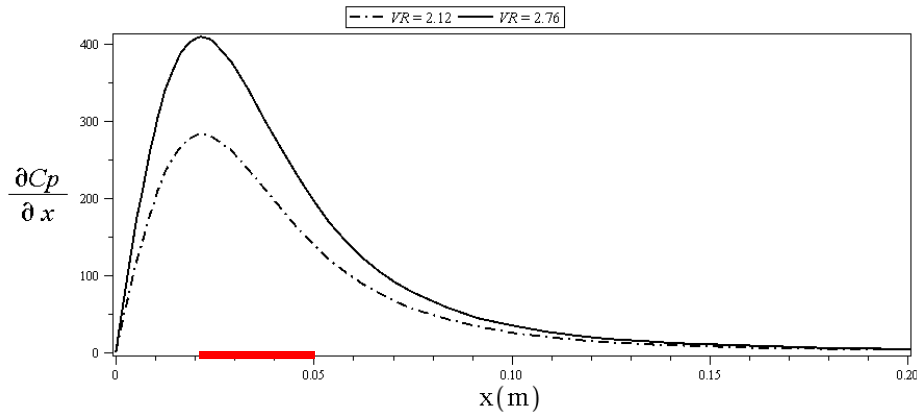


Figure 1.6: Potential flow estimate of the change in coefficient of pressure distribution over the flat plate under the two pressure gradients [1]

The flow over the plate was tripped turbulent upstream of the observation region. All experiments were carried out in the University of Alabama's low-turbulence water tunnel facility. The PIV image processing software, Insight, was used in the analysis of the results. Full field velocity contours, along with backflow coefficient contours, boundary layer profiles, Reynolds stresses, and turbulence intensity comparisons were used to quantify the results.

## 1.4 DEFINITIONS AND EQUATIONS

### 1.4.1 BACKFLOW COEFFICIENT

Backflow coefficient is defined as the percentage of time during the experiment that the flow at a specific point in the investigation window was moving counter to the free stream direction. It is calculated by summing the number of negative  $u$  velocity components that occur in the analyzed PIV images for each point, dividing that number by the total number of images, and multiplying by 100. The equation is shown in Equation 2.

$$\text{Backflow Coefficient} = \frac{\text{\# of vectors with negative } u \text{ velocity components}}{\text{total \# of vectors}} \times 100 \quad (2)$$

### 1.4.2 REYNOLDS NUMBER

The Reynolds number is defined in Equation 3.

$$Re = \frac{\rho u L}{\mu} \quad (3)$$

In this study, the density of water ( $\rho$ ) is  $1000 \text{ kg/m}^3$ , and the dynamic viscosity of water ( $\mu$ ) is  $1 \times 10^{-3} \text{ Ns/m}^2$ .

### 1.4.3 TURBULENCE INTENSITY

Turbulence intensity quantifies the amount of fluctuation about the average value of velocity at a given point in the flow. It is calculated as shown in Equation 4.

$$I = \frac{\sqrt{\frac{1}{2}(u'^2 + v'^2)}}{\sqrt{\bar{u}^2 + \bar{v}^2}} \quad (4)$$

#### 1.4.4 REYNOLDS STRESS

The dominant Reynolds stress in this shear flow is the product of the u and v components of the fluctuation about the average velocity at a given point. The definition is given by Equation 5.

$$\tau = \rho \overline{u'v'} \quad (5)$$

#### 1.4.5 VORTICITY

The vorticity of the flow is defined as the gradient of the velocity vector, and is given for 2D flow in Equation 6.

$$\xi = \nabla \times \vec{v} = \frac{\delta v}{\delta x} - \frac{\delta u}{\delta y} \quad (6)$$

## 2. REVIEW OF LITERATURE

### 2.1 TURBULENT BOUNDARY LAYERS

When a flow interacts with a surface, friction with that surface causes the flow in the region near that surface to decelerate. This region, beginning with the flow adjacent to a surface and ending at the point where the flow's velocity reaches 99% of the free stream velocity, is called the boundary layer. Turbulent boundary layers grow more rapidly than laminar boundary layers. As compared to laminar boundary layers their velocity profiles are steeper near the wall and shallower away from the wall. Within a turbulent boundary layer Reynolds stresses grow from zero at the wall to a peak near the wall, and diminish to zero as they approach the non-turbulent free stream flow. Similar trends are observed in the turbulent kinetic energy of a turbulent boundary layer. Flow within a turbulent boundary exhibits turbulent structures which are defined as coherent patterns in the turbulence that are significantly larger than the largest turbulent fluctuations. These structures include ejections of low speed fluid away from the wall, sweeps of high speed fluid towards the wall, and low speed streaks in the near wall region [13].

Djenidi [5] studied turbulent boundary layers over transverse square grooved surfaces and found that flow out of and in to the cavities corresponded with low speed streaks and high speed ejections respectively. He saw an increase in the Reynolds stresses and turbulence intensities within boundary layers over these surfaces as compared to smooth wall boundary layers. Djenidi theorized that the inflow and outflow of the cavities were exchanging momentum

between the cavities and the flow in the region above the wall, helping to stabilize the turbulent boundary layer. [5]

## 2.2 TURBULENT BOUNDARY LAYER SEPARATION

The nature of turbulent boundary layer separation has been the focus of much research in the field of fluid dynamics. Simpson [15] studied in depth the separation that occurred within a gradually decelerated turbulent flow. Simpson noted that the point at which the flow begins to intermittently reverse corresponds well to the location in the flow at which the pressure gradient in the free stream flow rapidly decreases. The mean flow within the separation region is on average the same magnitude or smaller than the turbulent velocity fluctuations within that same region. Angele [2] similarly studied boundary layer separation. He defined three types of separation: that caused by a mild adverse pressure gradient, that caused by a high adverse pressure gradient, and that caused by a sharp geometric feature. The high adverse pressure gradient case is characterized by large regions of separation with large curvatures in the streamlines, and high velocity backflows. This type of separation may reattach or may fully break away, forming a shear layer. Angele [2] studied the beginnings of separation induced by the mild adverse pressure gradient case. For this case they found no distinct point of separation, but rather intermittent separation occurring around a mean separation point. Figure 2.1 shows Angele's PIV images demonstrating the fluctuating nature of the backflow region within a boundary layer under a mild adverse pressure gradient. Large structures of reversing flow form and dissipate. The velocity at any point within the separation region can vary from positive to negative, and reversing regions upstream of the mean separation point can completely disappear. The features of the separation region are purely the result of time averaging. Figure 2.1 shows

several instantaneous PIV images of a region of turbulent boundary layer separation. In the image, black represents reversing flow. This figure shows the transient nature of turbulent boundary separation. The size and shape of the reversed region changes drastically from frame to frame. The separation region is shallow, with the backflow region near the wall. The separation is extremely sensitive to changes in upstream condition, making prediction of the point of separation difficult. Angele found that the boundary layer was able to resist high adverse pressure gradients in the early stages in its development, and becomes more sensitive as it develops. Under a zero pressure gradient the peak turbulence intensity occurred near the wall, but under the effects of an increasing adverse pressure gradient, the peak turbulence intensity moves up into the boundary layer until such a strong adverse pressure is achieved that the peak disappears and maximum variation in the u direction velocities occurs at close to 55% of the boundary layer height.

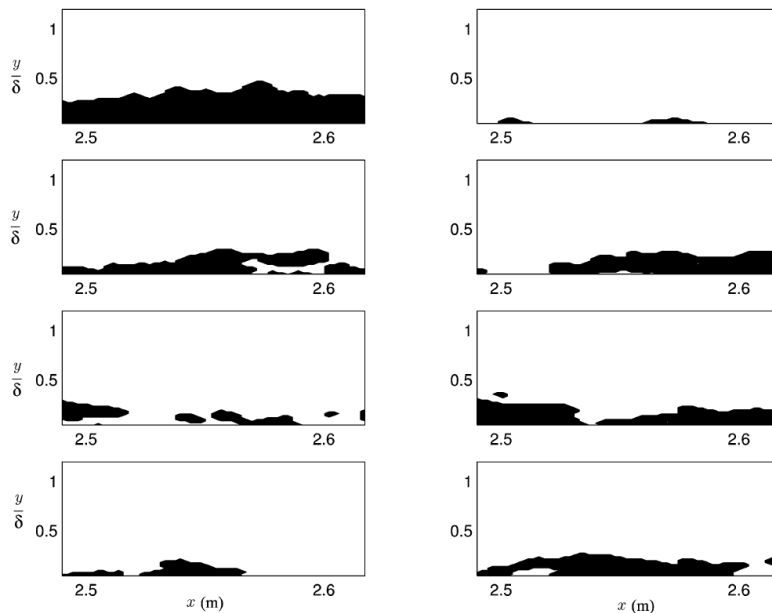


Figure 2.1: Fluctuating backflow region example images [2]

### 2.3 GENERATING AN ADVERSE PRESSURE GRADIENT

Physical limitations within the research setting make the generation and observation of adverse pressure gradients and their effects within a test region or a water or wind tunnel difficult. Traditional methods for doing so involve the alteration of the geometry of the test setup by creating a test region with decelerating flow. Control of a pressure gradient generated in such a way is difficult. Li [9] studied the possibility of using a cylinder to generate a local adverse pressure gradient. In low Reynolds number flow using dye visualization, Li observed that the presence of a stationary cylinder near a wall generates intermittent favorable and adverse pressure gradients, correlating with the vortex shedding in the cylinder's wake. Li found that spinning the cylinder such that the velocity of the cylinder's bottom point was in the direction of the flow created a sustained adverse pressure gradient. Figure 2.2 shows an image from Li's dye visualization study. He also noted that increasing the cylinder rotation speed increased the strength of the pressure gradient and moved its position closer to the cylinder. The cylinder's distance from the plate also affected the strength of the pressure gradient.

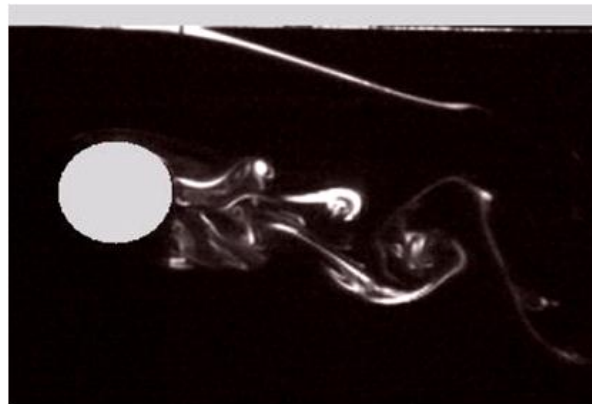


Figure 2.2: Dye visualization of separation on the flat plate above due to presence of spinning cylinder [9]

At The University of Alabama, Afroz [1] extended this adverse pressure generation technique to higher Reynolds number flow. She confirmed that the affect also existed in

turbulent flows, with similar relationships between the strength and location of the pressure gradient and the rotation and location of the cylinder at the higher Reynolds numbers indicative of turbulent flow. A spinning cylinder is used in this research to generate the adverse pressure gradients within the test region.

## 2.4 METHODS OF SEPARATION CONTROL

Much research has been devoted to the problem of delaying or preventing boundary layer separation. Methods to do so can be classified as either active or passive separation control techniques. Active separation control techniques are defined as methods to eliminate or delay boundary layer separation that expend energy in the process. Passive techniques rely on the geometry of the surface to control separation without the need for adding energy, and are therefore preferable to active techniques.

Howard [17] studied the effect of transverse embedded grooves of the drag characteristics of axisymmetric bluff bodies. He grooved these bodies circumferentially along their sharp trailing edges and observed the separated region as compared to a smooth surface bluff body. Howard theorized that these grooves would shed vortices into the boundary layer and act as a trip in the laminar flow. He did find a drag reduction due to a delay in boundary layer separation and reduction in size of the separation region. Howard observed that the grooves were able to keep the separation in smaller pockets, and delay the onset of a fully separated boundary layer.

Selby [14] examined the effect of a similarly transversely grooved surface on the separation of the boundary layer occurring over a backwards facing ramp in a wind tunnel. They saw a delay in boundary layer separation, and a decrease in the size of the separation region. They examined varying groove sizes and configurations, and found that below a certain depth to width ratio, there was a substantial increase in drag, indicating that a maximum groove width for

a positive effect in the flow. They also found that decreasing the size of the grooves too much would likewise eliminate the positive effect of the grooves presence, indicating that an optimum size exists. They noted an increase in the turbulent fluctuations within the boundary layer due to the grooves. Similarly, Loureiro [11] studied the effect of surface roughness on the separation region on backwards facing hills. He also found that surface roughness decreased the size of the separation region.

## 2.5 DOLPHIN AND SHARK SKIN

Biological surfaces have long been the inspiration for studies into possible drag reducing surfaces. A component of their potentially drag reducing affect can be attributed to the ability of these surface to passively delay boundary layer separation.

Shark's skin, and in particular the scales that grow over the skin like teeth, are understood to have a hydrodynamic benefit to the shark. Bruse [3] demonstrated that the grooves that run parallel to the flow direction that are present on the shark's scales act as riblets over its surface, decreasing drag by deterring cross flow. Lang [7] theorizes that the scales, which are loosely embedded in the shark's skin, are able to erect in the presence of reversing flow due to an adverse pressure gradient, trapping the reversing flow and forming transverse grooves with embedded vortices between them.

In the 1930's, Sir J. Grey studied the biology of dolphins, their swimming speeds and drag over their bodies. He concluded that the propulsion produced by a dolphin was infeasible. Either a dolphin's muscles are seven times more powerful per unit mass than any the muscles of any other mammal, or a dolphin is able to maintain laminar flow over its body by some extraordinary means. This phenomenon has come to be known as Grey's Paradox [6]. Several

errors in Grey's calculations have since been discovered. Primarily he erred in using the muscle power values for endurance performance in human rowers, while using the swimming speeds of dolphins achieved during short bursts. It is well known that muscles can produce much more power during a short burst as opposed to a long duration motion; however, dolphins are still acknowledged to be extraordinarily efficient swimmers [6].

Fish [6] examined potential mechanisms for drag reduction employed by dolphins. He noted that the dolphin body shape is a highly streamlined body, mimicked in submarine design, which is a likely contributor to the dolphins lower than expected drag. However, Fish noted that observations of live dolphins swimming show little to no separation over their bodies, while duplicates of their body shape can be observed to have separation occurring over their surfaces. He notes that their body shape cannot be solely responsible for their efficiency. It is theorized that a dolphin's skins acts as a compliant wall, employing viscous damping to reduce drag. Their skin may absorb perturbations in the boundary layer that would ordinarily lead to a transition to turbulent flow. By delaying this transition the dolphin's skin reduces drag over its surface. Research into this affect has shown that the unique relationship between the epidermis and dermis of the dolphin's skin can absorb up to 95% of turbulent perturbations. Still, given its speed and the movement of its swimming motion, it is unlikely that the dolphin is able to maintain a fully turbulent flow over its entire body. Fish notes that a dolphin's skin is covered in embedded circumferential grooves ranging from .41 to 2.35 mm in width and 7 to 114 mm in height. These grooves are believed to have a function in the nervous system of the dolphin, making the skin more sensitive. He speculated that these grooves could also have a positive hydrodynamic for the dolphin.

The presence of the embedded transverse grooves on the skin of sharks and dolphins, combined with the theory that such grooves may have a positive aerodynamic benefit in the presence of an adverse pressure gradient, was the inspiration for this research, which seeks to further understand the nature of this affect and its origins within the flow.

### 3. EXPERIMENTAL SETUP

#### 3.1 EXPERIMENTAL FACILITY

This research was conducted in the low turbulence water tunnel in the Aerospace Engineering Department at the University of Alabama. The water tunnel is a modified version of the Eidetics Model 1520 tunnel manufactured by Rolling Hills Research Corporation. Designated 1520-EXT, indicating an extended test section, the water tunnel has been modified to have a 108 inch long and 30 inch high test section with a width beginning at 16.25 inches and increasing to 17.25 inches over the length of the test section in order to account for the growth of the boundary layer displacement thickness. The total volume of the tunnel is slightly larger than 1000 gallons, and the highest achievable free stream velocity in this tunnel is approximately 0.5 m/s in the test section. The water tunnel has been installed with a high performance impeller, which is driven by a 2.0 horsepower, 230 V, 3-phase electric motor with a frequency range of 0-60 Hz.

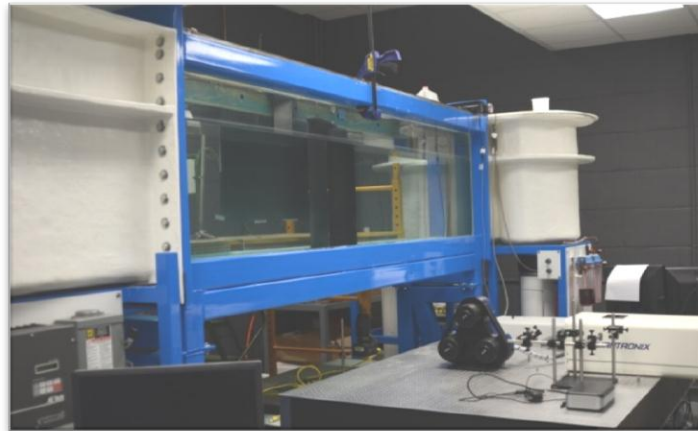


Figure 3.1 University of Alabama water tunnel facility

### 3.2 EXPERIMENTAL MODEL

The model used in this experiment is a flat acrylic plate model with an interchangeable middle section as shown in Figure 3.2. Axes used to display the orientation of the model are labeled as follows: x is positive downstream, y is positive toward the laser, and z is positive up. Beginning with a tapered leading edge, 36 inches (91.44 cm) of flat plate precede the 24 inch (60.96 cm) interchangeable section, and 24 inches (60.96 cm) follow it. The last 9 inches (22.86 cm) of the model are hinged into a tapered trailing edge section which can be adjusted to ensure attached flow over the test section. The dimensions of the plate are shown in Figure 3.3. This model is mounted into the water tunnel from above, and held in place with connections to three L-beams which rest on top of and span the width of the tunnel. The model is located in the middle of the available test section, with 11 inches (27.94 cm) of water between the model surface and the side of the test section. The interchangeable section sits on two stainless steel bars that connect the sections preceding and following it which can be tightened and loosened with counter sunk screw connections. In this way, the model section can be changed without the disruption of the tunnel operation. The adverse pressure gradient is generated over the plate with the use of a spinning PVC cylinder that reaches the entire height of the test section and is located 2 cm above the plate. The cylinder is 2.05 inches (5.207 cm) in diameter and is operated by a JVL integrated stepping motor, model MIS 231. The motor is controlled via MacTalk software. The cylinder and rectangular grooved model were fabricated in The University of Alabama Engineering Machine Shop, along with the mount for the sinusoidal grooved model. The sinusoidal model was 3D printed in two sections and screwed into the mount.

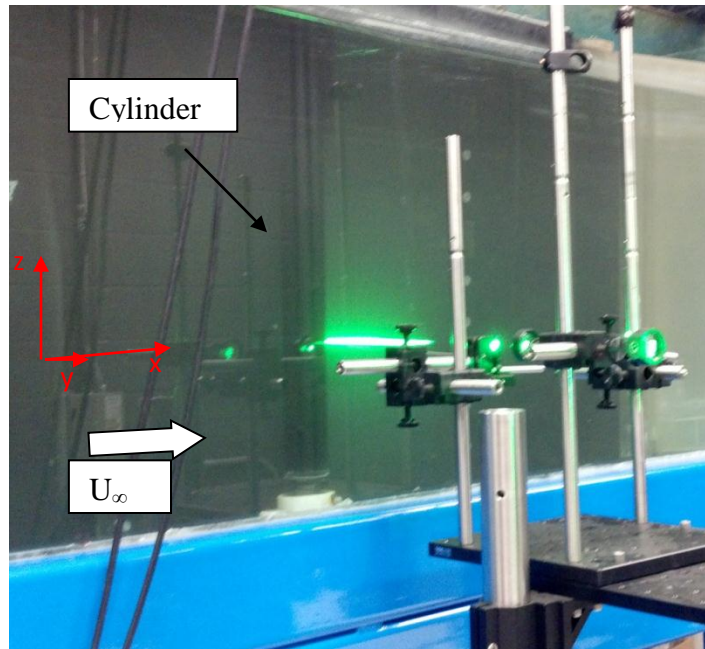


Figure 3.2 Image of flat plate model and cylinder in the water tunnel during a test

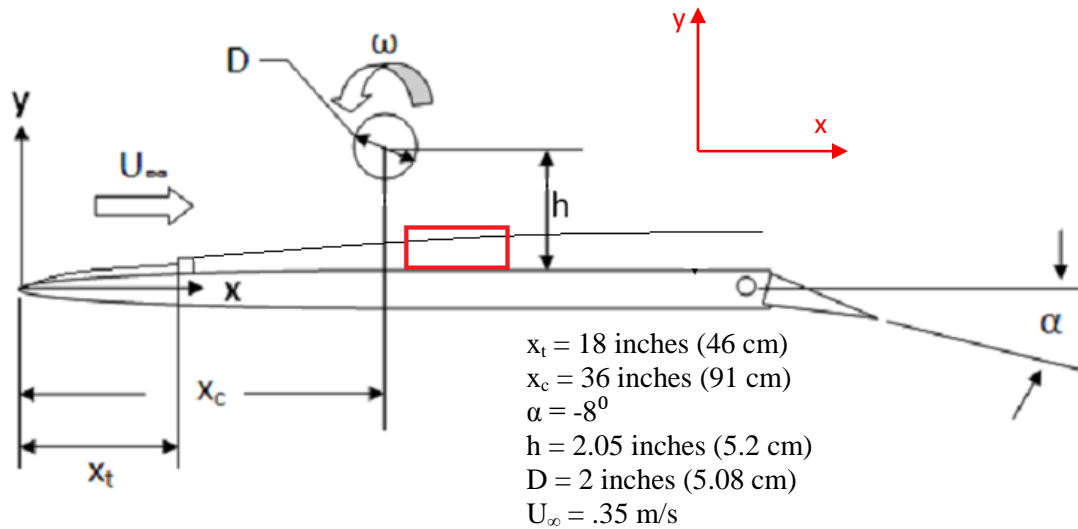


Figure 3.3 Model of experimental setup

The three model plates manufactured for this experimental were machined from a 2 inch thick acrylic sheet with a CNC machine. One model was manufactured flat, one with 2 mm by 3 mm rectangular embedded grooves running the length of the plate, and one with pseudo-

sinusoidal embedded grooves, measuring 3 mm in width and 1 mm in height. The cavity Reynolds number based on the 2 mm width of the cavities is 630.

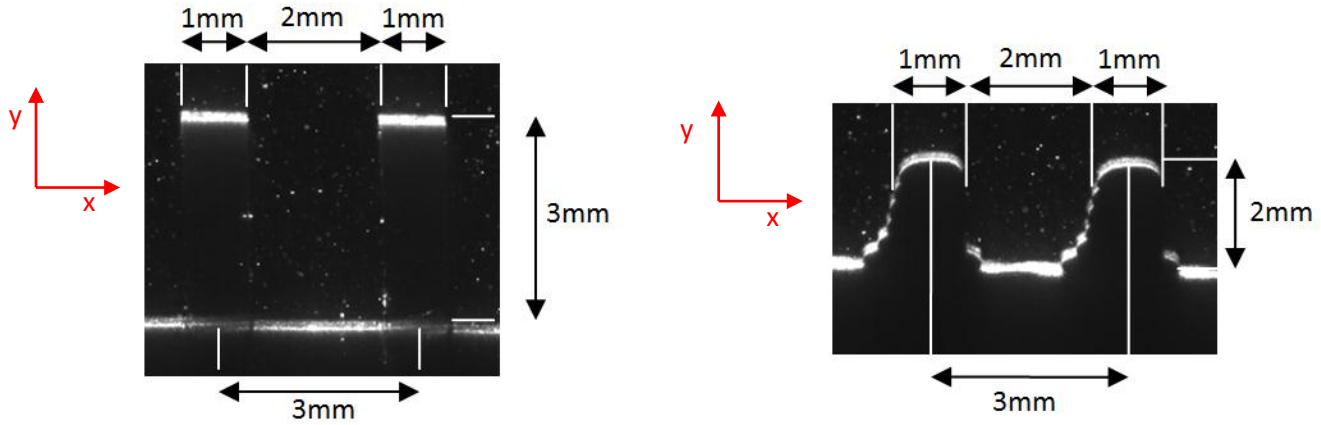


Figure 3.4 Diagram of model sections

### 3.3 DPIV SYSTEM

The data for this research were acquired with a two dimensional time-resolved digital particle image velocimetry system consisting of a pulsed solid-state laser, a high speed digital camera, image acquisition software, and DPIV processing software. A Falcon 30 series Nd:YLF Quantronix Corporation laser was used in this setup. This laser's maximum power output is 20 watts, beam wavelength of 532 nm, 7 to 30 amps current output range, and .1 to 1.0 kHz frequency range. The laser operates at a temperature between 27°C and 31°C, and is externally water-cooled. It is fired through an optic array that expands the beam into a laser sheet which illuminates a plane of the flow over the test section. A diagram of the data capture setup is shown in Figure 3.5. The water inside the tunnel is seeded with neutrally buoyant 15 micron diameter

hollow glass spheres coated in silver. These particles are illuminated as they pass through the laser sheet. Matching the frame rate of the camera with the pulse rate of the laser, images of these illuminated particles are captured at 1000 frames per second by a Basler high-speed camera at 1280x512 pixel resolution. The camera was located under the test section, and positioned such that it was looking up into the flow. Images of the laser and camera are shown in Figure 3.6. These images are acquired via a Labview program and imported in Insight 3G PIV processing software developed by TSI, Incorporated.

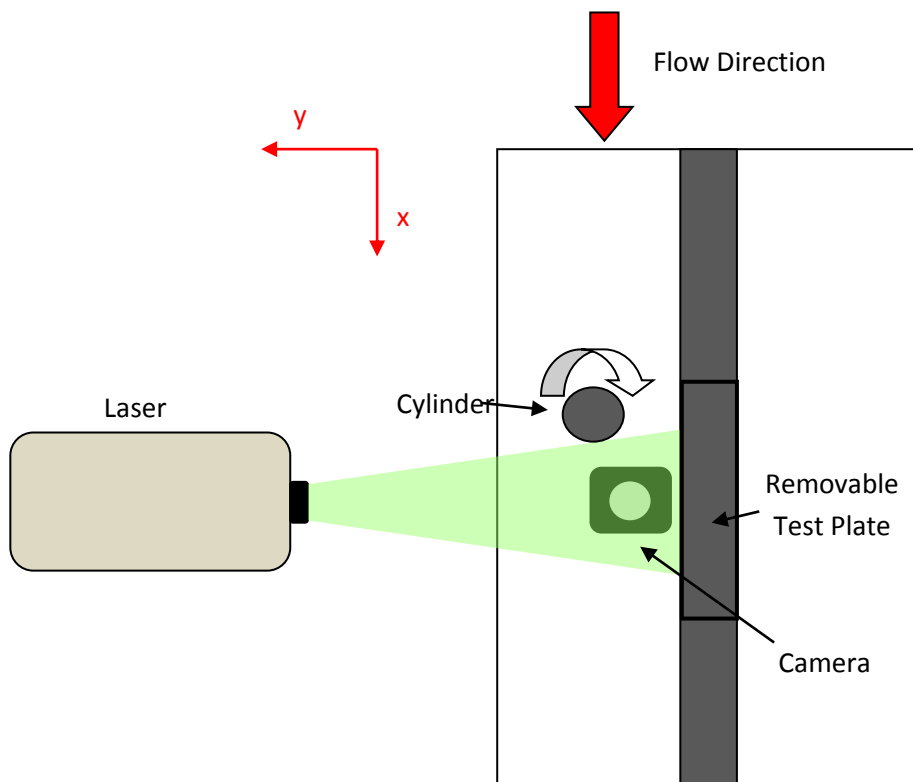


Figure 3.5 Diagram of Data Capture Setup



Figure 3.6 Images of (a) Basler high speed camera and (b) Quantronix pulsed laser

### 3.4 EXPERIMENTAL PROCEDURE

Data were taken with a water tunnel impeller frequency of 30 Hz, corresponding to a tunnel free stream speed of approximately .25 m/s. For each combination of pressure gradient and plate geometry investigated 10,000 images were taken at a frame rate of 1000 frames per second. Baseline data were taken over the flat plate, and both grooved models without any adverse pressure gradient and without the presence of the cylinder in the tunnel. Primary experimental data consisted of 2 different adverse pressure gradients. Cylinder rotation speeds of 200 RPM and 260 RPM corresponding to non-dimensional rotational velocities of 2.12 and 2.76. The camera was positioned such that the flat plate was barely within the bottom of the image. The data window is 3 cm long by 1.5 cm in height. This window is the smallest investigation window possible with the experimental setup used in these experiments. As the focus of this research was to examine the interaction of flow within the grooves embedded in the surface, the highest resolution of flow in and directly above the cavities possible was desired. It is important to note that theoretical calculations of the boundary layer height at the point of observation predict a boundary layer height of 2.7 centimeters; therefore the entire boundary layer is not captured in this data. The investigation window begins directly 2.05 cm downstream of the

midpoint of the cylinder. When taking data over the grooved surfaces, the camera window was adjusted such that the entirety of the interior of the embedded grooves was within the window.

TSI, Incorporated Insight 3G DPIV processing software was used in the analysis of the images taken during the experiments. The images are processed as time resolved, meaning the first and second images are paired for the first vector calculation, and the second and third are paired for the second, and so on. A minimum intensity image generator is used to determine the background noise common to all of the images, and this noise is subtracted from all of the images to increase the accuracy of the vector calculations. During processing, Insight was set to perform classic PIV using a Recursive Nyquist Grid, FFT Correlation Engine, and Gaussian Peak Engine. The particle window size began at 64x32 pixels, and was reduced to 16X8 pixels, with a maximum displacement of .4 the window size in both the x and y directions. Adequate tunnel seeding was ensured by taking single test images of the illuminated observation window and manually counting the number of particles that appear within several 16X8 pixel windows. This pixel window was chosen as it is the final processing grid size. For accurate PIV data, 5 to 8 particles should appear inside each of these windows. To ensure adequate camera frame rate, image pairs are taken and the pixel displacement of several particles are measured. The maximum displacement cannot exceed the 40% of the width of the processing grid window which is 6 pixels. Insight generated vector files containing full field U and V velocity components for each image pair, and further analysis was performed using in house MATLAB codes. A demonstration of the final processed grid is shown over an example flat plate image in Figure 3.7.

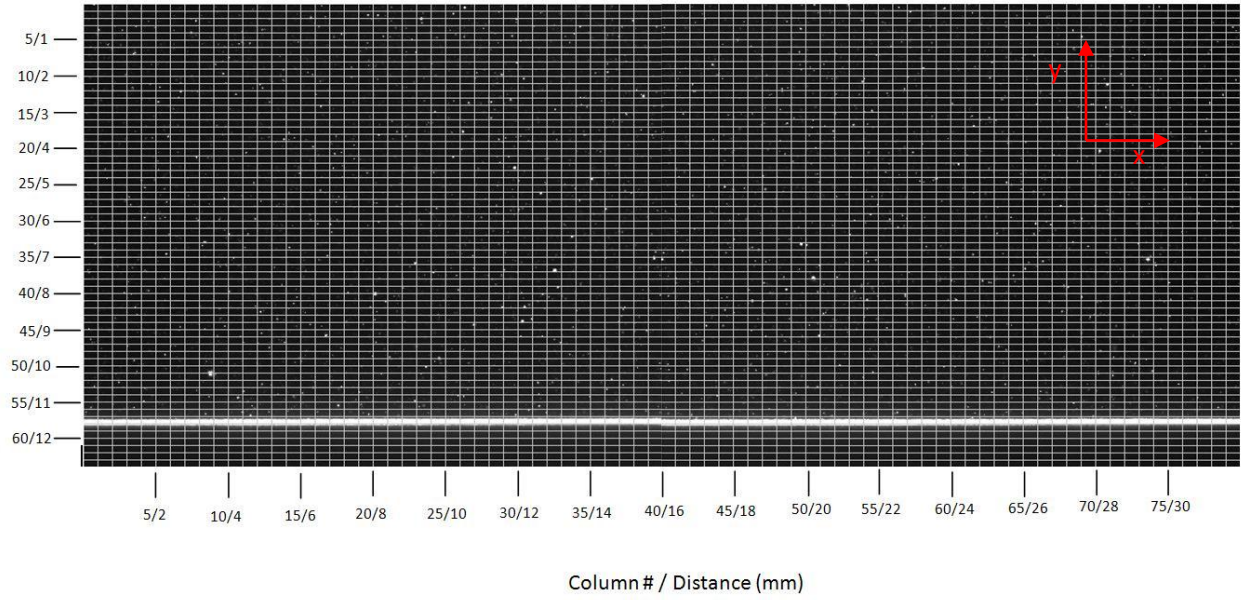
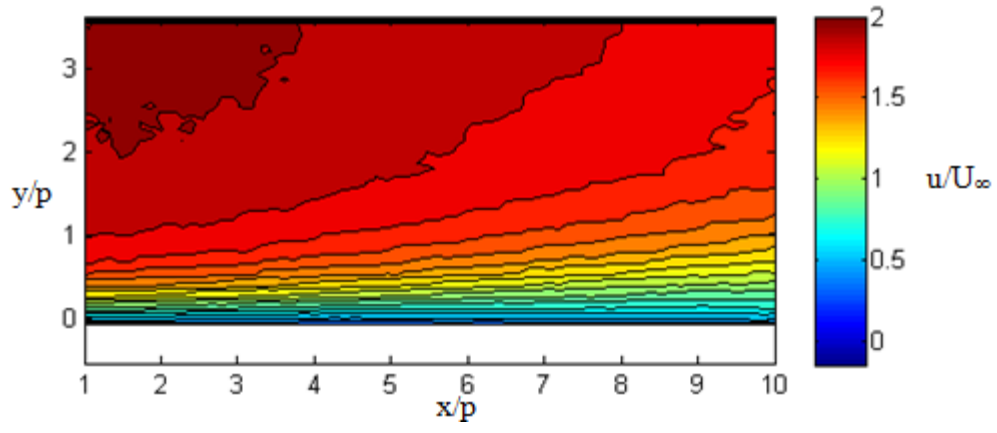


Figure 3.7: Example Final Processed Grid

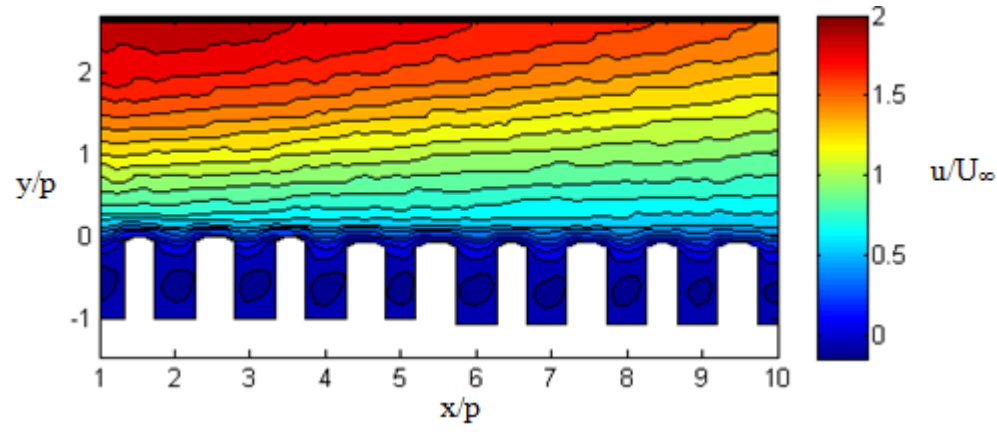
## 4. RESULTS AND DISCUSSION

### 4.1 MEAN $u$ VELOCITY FIELD CONTOUR COMPARISON

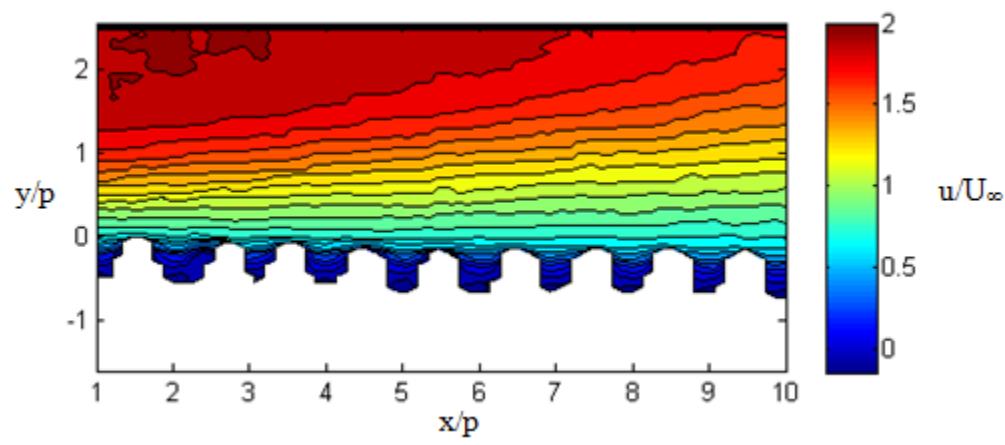
Each data set consists of 10,000 images taken at 1000 frames per second. Mean  $u$  velocity contours of the 10,000 image averages for each plate at each pressure gradient and the no pressure gradient case were generated. Figure 4.1 shows these averages for each plate at the first pressure gradient. Appendix A.1 shows this comparison under the second pressure gradient. The  $x$  and  $y$  direction length measurements are non-dimensionalized by the period of the grooves ( $p = 3$  mm), and the velocity values are non-dimensionalized by the tunnel free stream velocity ( $U = .25$  m/s). Due to the transient nature of the reversing flow over the flat plate, and its slow velocity as compared to the non-reversed flow, the separation region is not seen in the 10,000 image average. In the average of the grooved and flat plates, the areas of negative velocity flow can be seen inside the cavities, revealing the bottoms of the consistently clockwise rotating imbedded vortices. The partial slips over the cavities can also be seen as the contours of velocity dip into each of the imbedded grooves. Although the entire boundary layer is not captured with the viewing window, the velocity contours show the growth of the boundary layer over the investigation region, and demonstrate the gradient of velocity within the boundary layer over length of the viewing window. It can be seen this gradient is higher over the sinusoidal surface as compared to the rectangular grooved surface.



(a)



(b)



(c)

Figure 4.1: Comparison of  $u$  velocity averages of 10,000 images of the (a) flat plate, (b) rectangular grooved plate, and (c) sinusoidal grooved plate

## 4.2 MEAN VELOCITY PROFILE COMPARISON

Due to the blockage effects of the cylinder's presence in the test section, values of velocity within the boundary layer exceed that of the tunnel free stream value. To examine the effect of the cylinder's presence on the boundary layer, The theoretical  $1/7^{\text{th}}$  power layer turbulent boundary layer profile is compared to boundary layer profiles over the flat plate with and without the presence of the cylinder. This comparison is shown in Figure 4.2. Figure 4.2 also shows the comparison of the three surfaces in the absence of a pressure gradient but with the presence of the cylinder. A straight line at  $y = 0$  indicates the top of the grooves and the location of the flat plate, which are aligned. The imbedded vortices of the rectangular and sinusoidal grooved surfaces can be seen below the  $y=0$  line. The rectangular grooved imbedded vortex can be seen to be stronger and larger than the sinusoidal surface imbedded groove in this case. The partial slip is seen to be roughly equivalent between the two grooved surfaces, and above the surfaces the three velocity profiles do not deviate significantly.

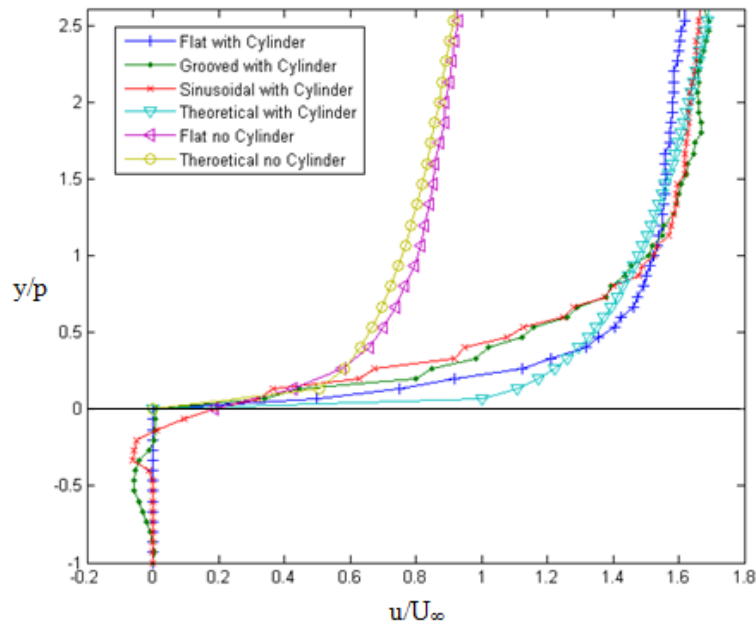
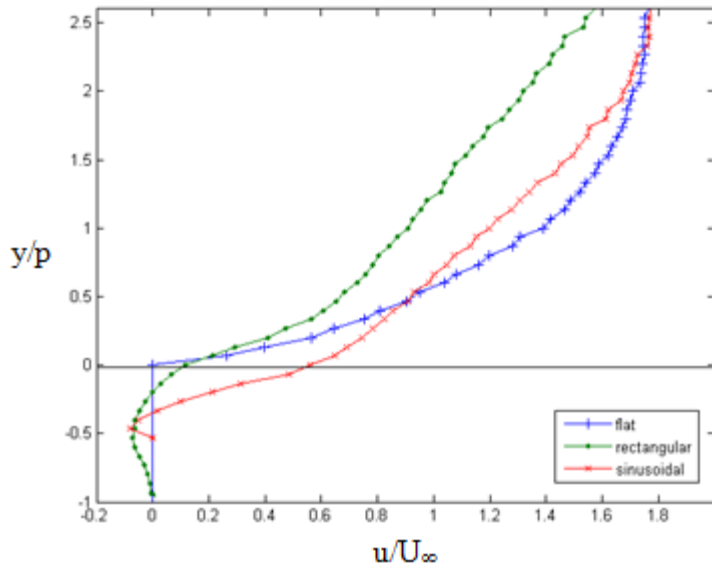
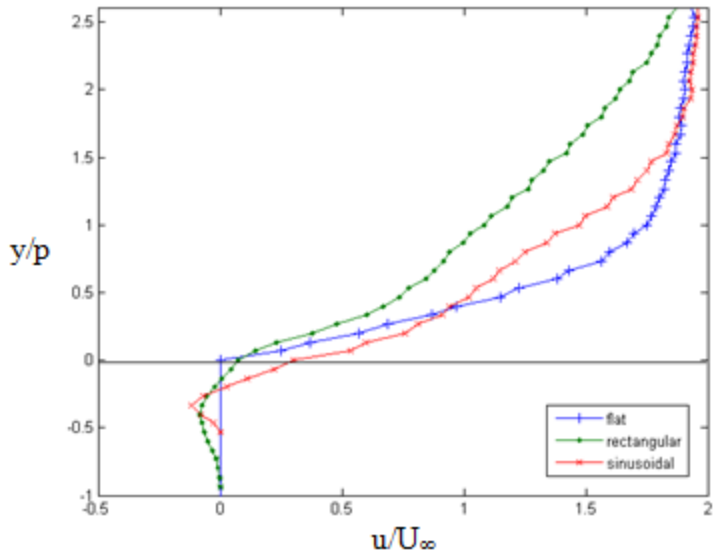
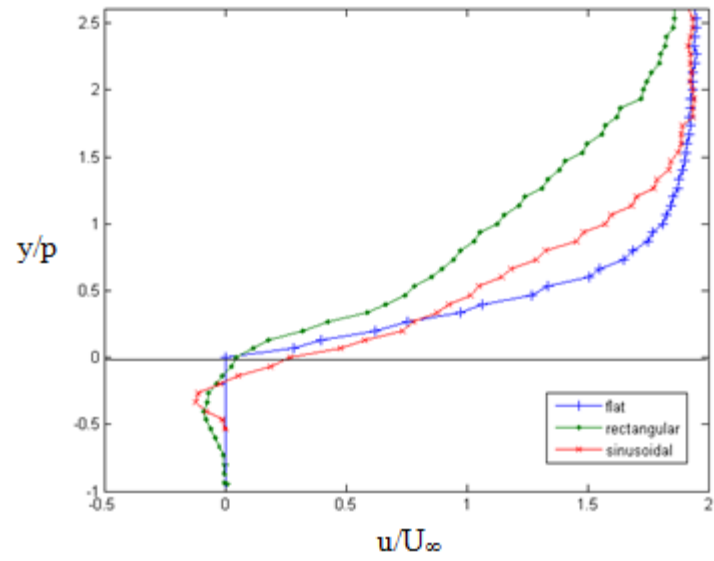
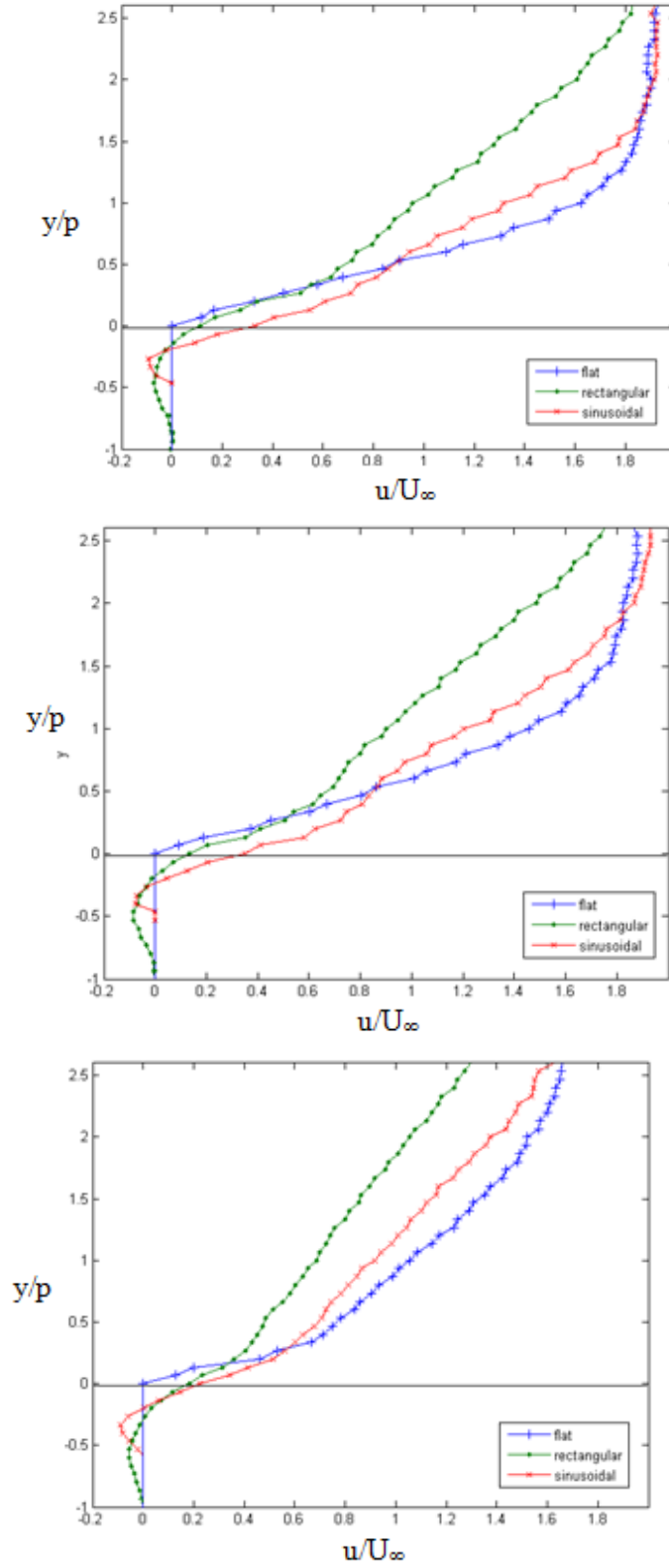


Figure 4.2: Velocity Profile Comparison of the Three Plates Without the Presence of a Pressure Gradient

For each of the pressure gradient cases, the velocity profiles over each of the three surfaces at three different locations in the investigation window are compared. Each of these locations was chosen to demonstrate a velocity profile through the center of a groove. Figures 4.3(a) and 4.3(b) show the velocity profile comparisons between the three surfaces under the first and second pressure gradient respectively at three locations within the investigation window. These locations were chosen as they represent the velocity profile through the middle of the first, third and ninth grooves fully visible within the investigation window. The profiles for the first pressure gradient show that the negative velocities induced by the vortex imbedded within the sinusoidal grooved surface are as strong as those imbedded within the rectangular grooved surface and the vortices embedded with the sinusoidal surface induce a larger partial slip than is seen over the rectangles. The imbedded vortices within both the rectangular and sinusoidal grooved surfaces appear to move farther into the groove and become more compact in the grooves farther downstream. The velocity profiles over the rectangular grooved surface are significantly more shallow than that of the flat and sinusoidal grooved surface, indicating a more rapid loss of momentum inside the boundary layer. Differing from the rectangular plate, the sinusoidal surface velocity profiles show a closer match to the velocity gradient of the flat plate profiles. The momentum is more efficiently conserved over the sinusoidal surface, which indicates lower drag over the sinusoidal surface as compared to the grooved surface, and drag comparable to that over the flat plate.



(a)



(b)

Figure 4.3: Comparison of velocity profiles over the three plates at three downstream locations under (a) the first and (b) the second adverse pressure gradients

### 4.3 PARTIAL SLIP ANALYSIS AND COMPARISON

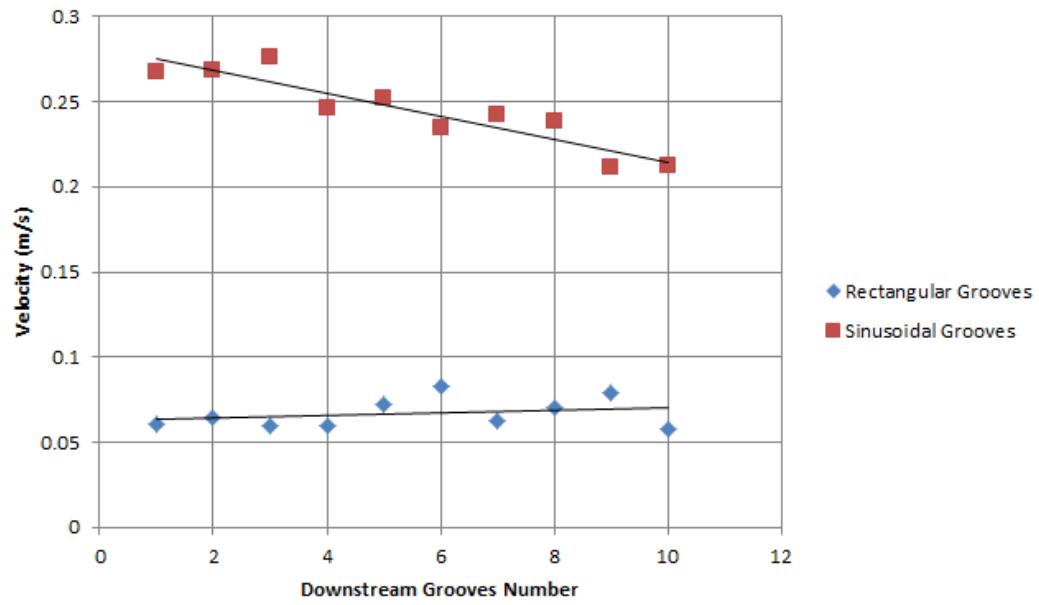
For the two adverse pressure gradient cases, the partial slips over each of the 10 grooves visible within the investigation window for both the rectangular and sinusoidal grooved surfaces are tabulated in Table 4.1, and plotted in Figure 4.4. The partial slips over the sinusoidal surface are consistently higher than those over the rectangular surface. Table 4.2 shows the average partial slip of the two surfaces under the two pressure gradients as percentages of the free stream velocity.

Table 4.1: Comparison of slip velocities over the rectangular and sinusoidal grooved plates under the two adverse pressure gradients

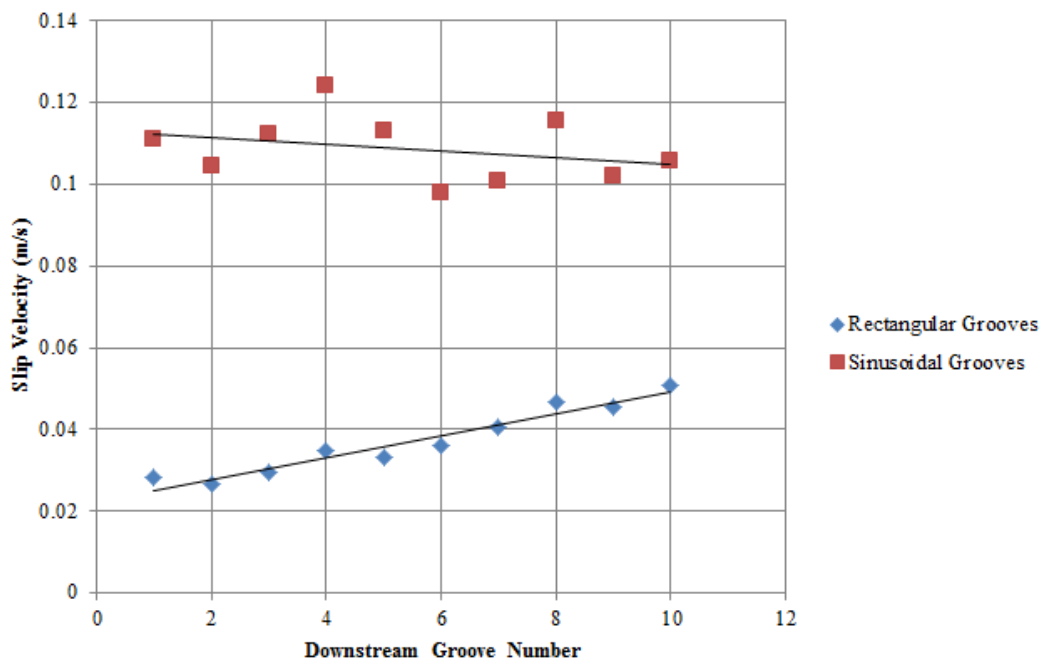
Grove #	Slip Velocity (m/s)					
	No Pressure Gradient		First Pressure Gradient		Second Pressure Gradient	
	Rectangular	Sinusoid	Rectangular	Sinusoid	Rectangular	Sinusoid
1	.06	.27	0.03	0.11	0.04	0.08
2	.07	.27	0.03	0.11	0.04	0.07
3	.06	.28	0.03	0.11	0.04	0.07
4	.06	.25	0.04	0.12	0.04	0.06
5	.07	.25	0.03	0.11	0.05	0.07
6	.08	.23	0.04	0.10	0.06	0.06
7	.06	.24	0.04	0.10	0.05	0.06
8	.07	.24	0.05	0.12	0.05	0.06
9	.07	.21	0.05	0.10	0.05	0.05
10	.05	.21	0.05	0.11	0.05	0.06

Table 4.2: Percent average slip velocities over the rectangular and sinusoidal grooved plates under the two average pressure gradients

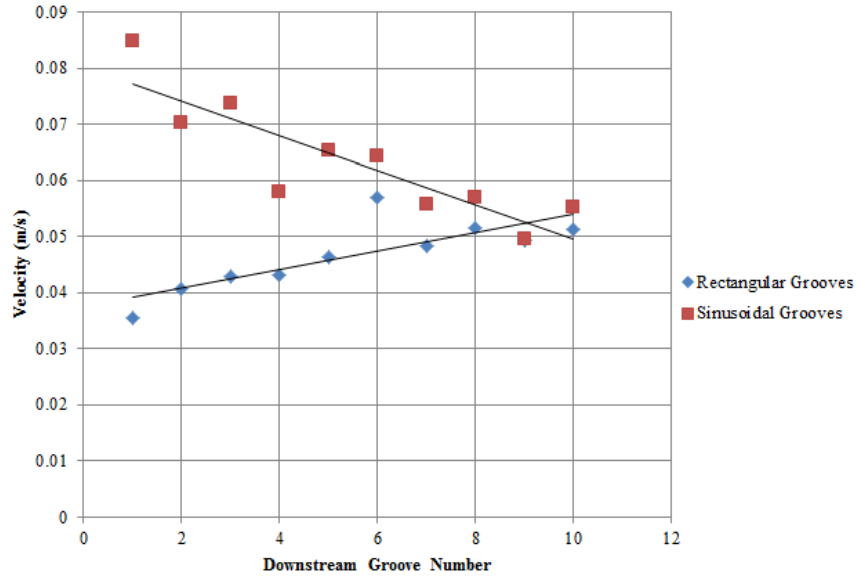
		Average Slip (m/s)	Percentage of Free Stream (%)
No Pressure Gradient	Rectangular	.07	16
	Sinusoid	.25	44
1 <sup>st</sup> Pressure Gradient	Rectangular	.04	8
	Sinusoid	.11	22
2 <sup>nd</sup> Pressure Gradient	Rectangular	.05	9
	Sinusoid	.06	13



(a)



(b)



(c)

Figure 4.4: Plots of the slip velocities over the rectangular and rectangular grooves under (a) no pressure gradient (b) the first pressure gradient and (b) the second pressure gradient

#### 4.4 BACKFLOW COEFFICIENT CONTOURS

The backflow coefficient is defined as the percentage of the total time that the flow is reversed. Backflow coefficient contours for the three surfaces under the two pressure gradients were generated. The backflow contours over the flat plate under the first and second pressure gradients are compared in Figure 4.5. The contours over the flat plate under the first pressure gradient show the transient separation induced by the pressure gradient. The separation over the flat plate induced by the second, higher, pressure gradient can be seen to be thicker and more sustained, with regions of 70% and 80% backflow.

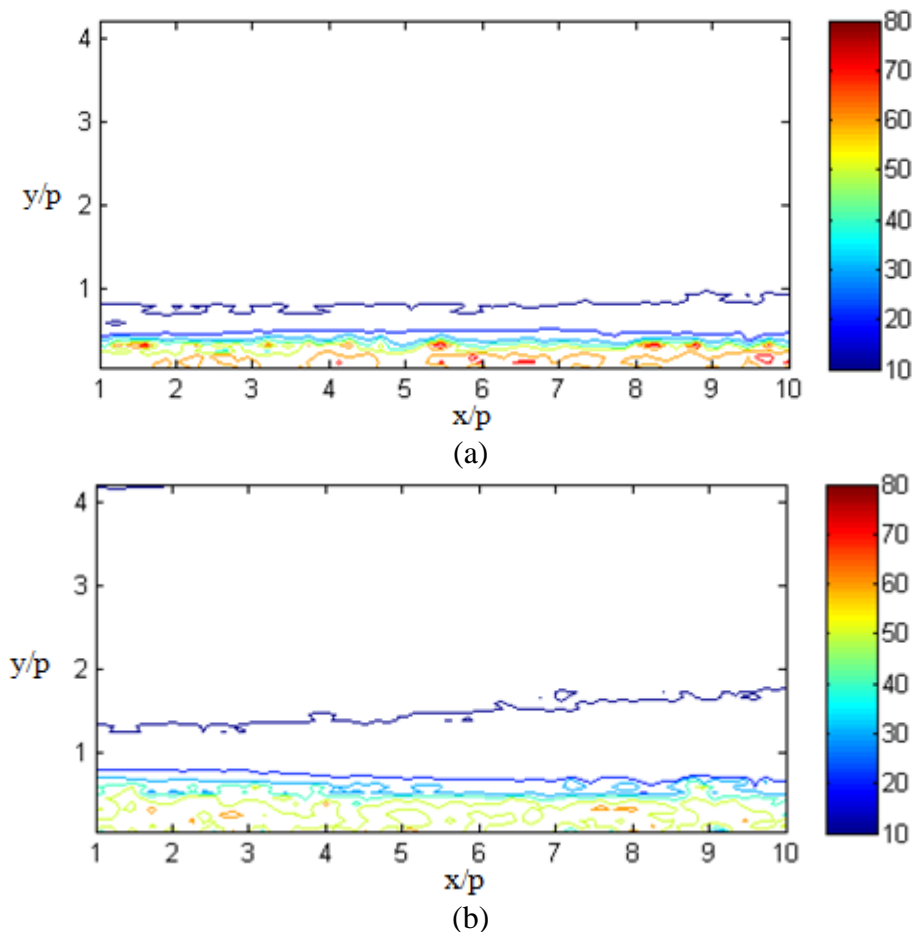


Figure 4.5: Comparison of backflow coefficient over the flat plate under (a) the first and (b) the second pressure gradient

Figure 4.6 shows the backflow contours over the rectangular and sinusoidal grooved surfaces under the second pressure gradient. Contours for the first pressure gradient can be seen in Appendix A.2. No region of reversing flow is seen over either of these surfaces. The sustained imbedded vortices can be seen within the grooves for both surfaces. The vortices imbedded within the rectangular grooved surface can be seen to be larger than those of the sinusoidal grooved surface. A large region of 10% backflow exists over both surfaces, indicative of the turbulence within the boundary layer.

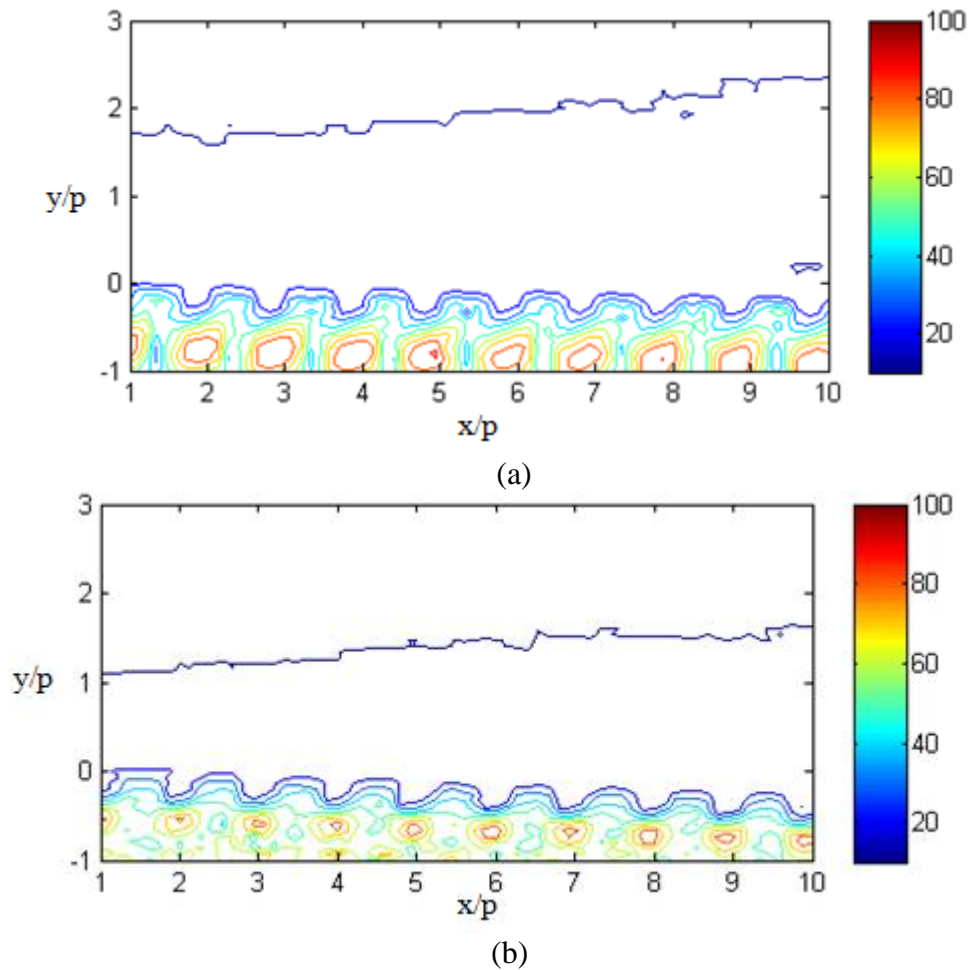


Figure 4.6: Comparison of backflow coefficient over the (a) rectangular and (b) sinusoidal grooved plates under the second pressure gradient

#### 4.5 TRANSIENT BOUNDARY LAYER SEPARATION OVER THE FLAT PLATE

Figure 4.7 shows a series of consecutive averages of 50 images depicting a time period in the experimental data in which the transient separation of the flat plate can be seen. This series was taken over the flat plate under the 2<sup>nd</sup> pressure gradient. Reversing flow is shown in white. As can be seen, the region of separation enters the investigation window, appearing under a growing region of slow moving flow. The beginning of the separation region travels upstream, and then retreats downstream again.

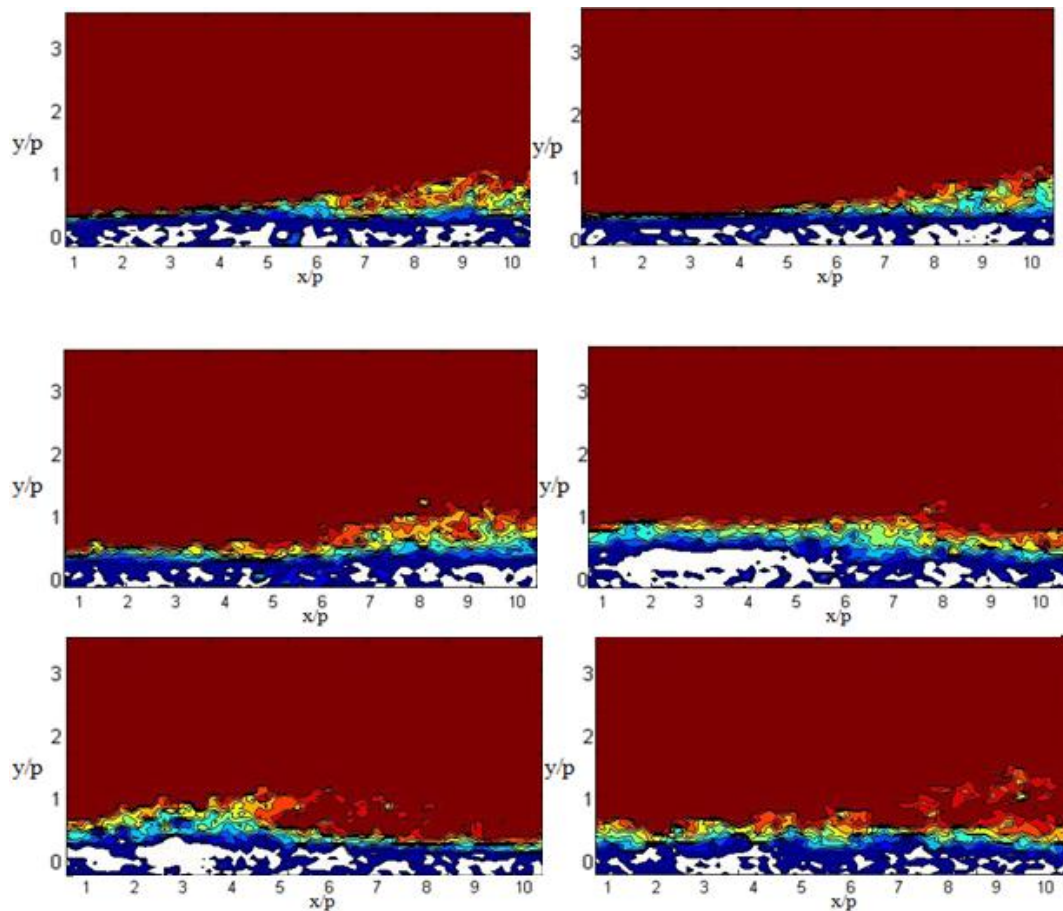


Figure 4.7: Series of  $u$  velocity averages demonstrating the transient nature of turbulent separation over the flat plate

#### 4.6 MEAN REYNOLDS STRESS FIELD

The Reynolds stresses for each of the surfaces under both adverse pressure gradients were calculated. Figure 4.7 shows in Reynolds stress contours for the first pressure gradient.

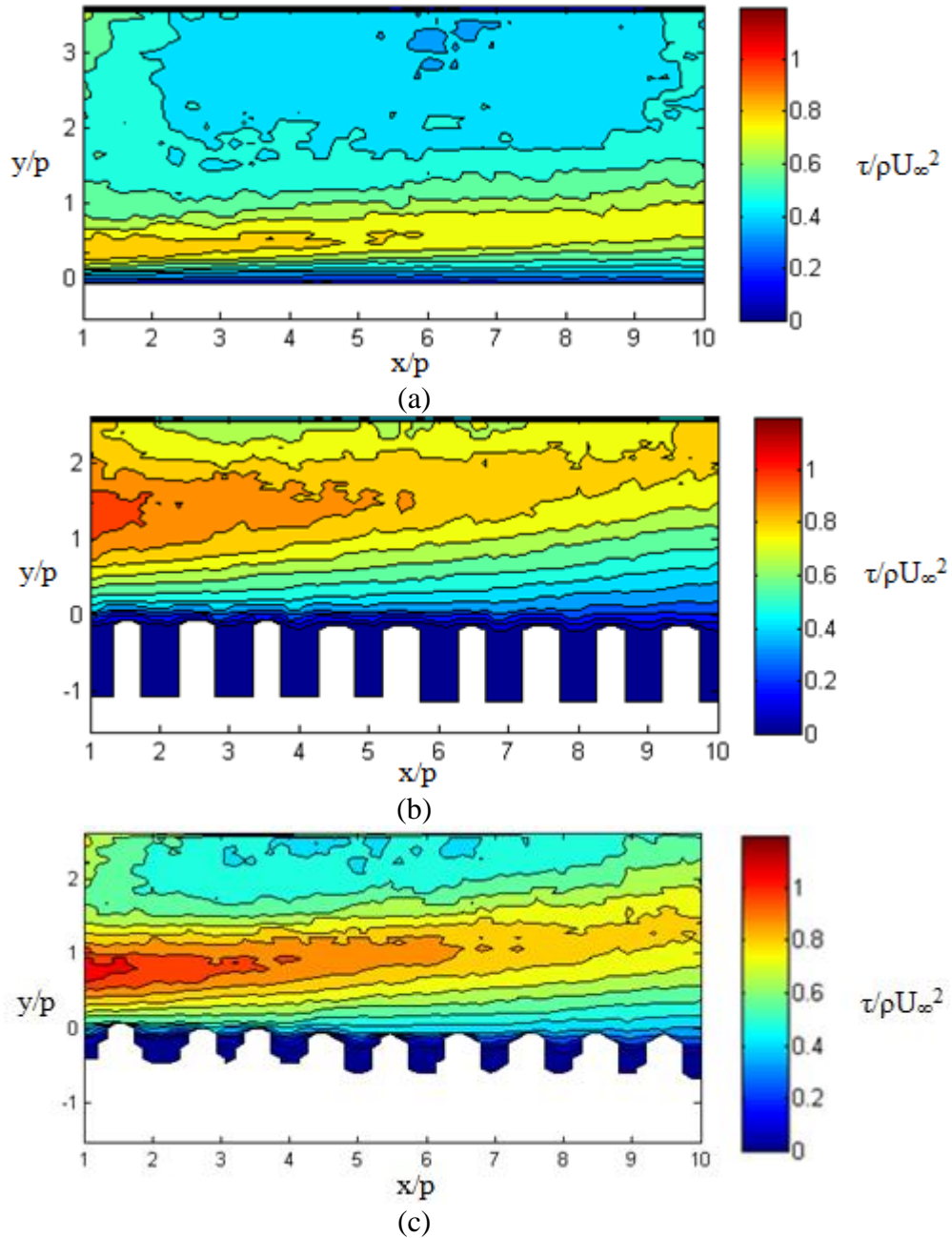


Figure 4.7: Comparison of Reynolds stress over the (a) flat plate, (b) grooved plate, and (c) sinusoidal plate at the first pressure gradient

Contours for the second pressure gradient can be seen in Appendix A.3. The Reynolds stresses are non-dimensionalized by dividing by the square of the free stream velocity and the water density. Indicative of the amount of fluid mixing present in the flow, high values of Reynolds stress occur in regions where high momentum fluid is moving down or low momentum fluid is moving up, and quantify momentum conservation in a flow. As can be seen in the Reynolds stress contours, the sinusoidal grooved surface shows the highest region of Reynolds stress which is located closer to the surface than that which occurs over the grooved surface.

#### 4.7 MEAN REYNOLDS STRESS PROFILE COMPARISON

To further examine the trends present in the Reynolds stresses, Reynolds stress profiles for the different surfaces are compared for the three pressure gradient cases. The data points for these profiles begin at the surface of the flat plate and tops of the grooves. Figure 4.8 shows a comparison of the Reynolds stress profiles for the three surfaces with the presence of a pressure gradient. As can be seen, the rectangular and sinusoidal grooved surfaces exhibit comparable Reynolds stress trends, both generating greater Reynolds stresses than exist over the flat plate.

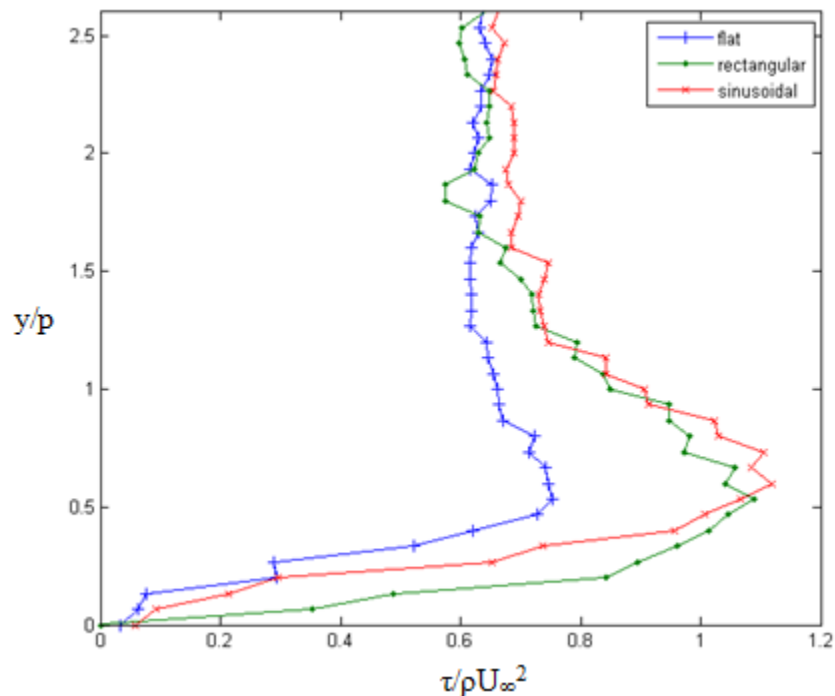


Figure 4.8: Comparison of the Reynolds stress profiles over the three plate geometries in the absence of a pressure gradient

Figures 4.9 and 4.10 show comparisons at three downstream locations of the Reynolds stress profiles for each of the three surfaces under the first and second pressure gradient respectively. Consistently, the grooved surfaces show higher maximum Reynolds stresses than the flat plate, with the sinusoidal grooved plate producing slightly higher maximum Reynolds

stresses than the rectangular grooved plate. The height of the maximum Reynolds stress rises over the length of the plate for all three surfaces. The maximum Reynolds stress height is consistently lower for the sinusoidal grooved surface than for the rectangular grooved surface, suggesting better mixing closer to the wall over the sinusoidal grooved surface. It is interesting to note that in the region of the flow closer to the wall, the grooved surface appears to induce less mixing of the flow than the flat plate.

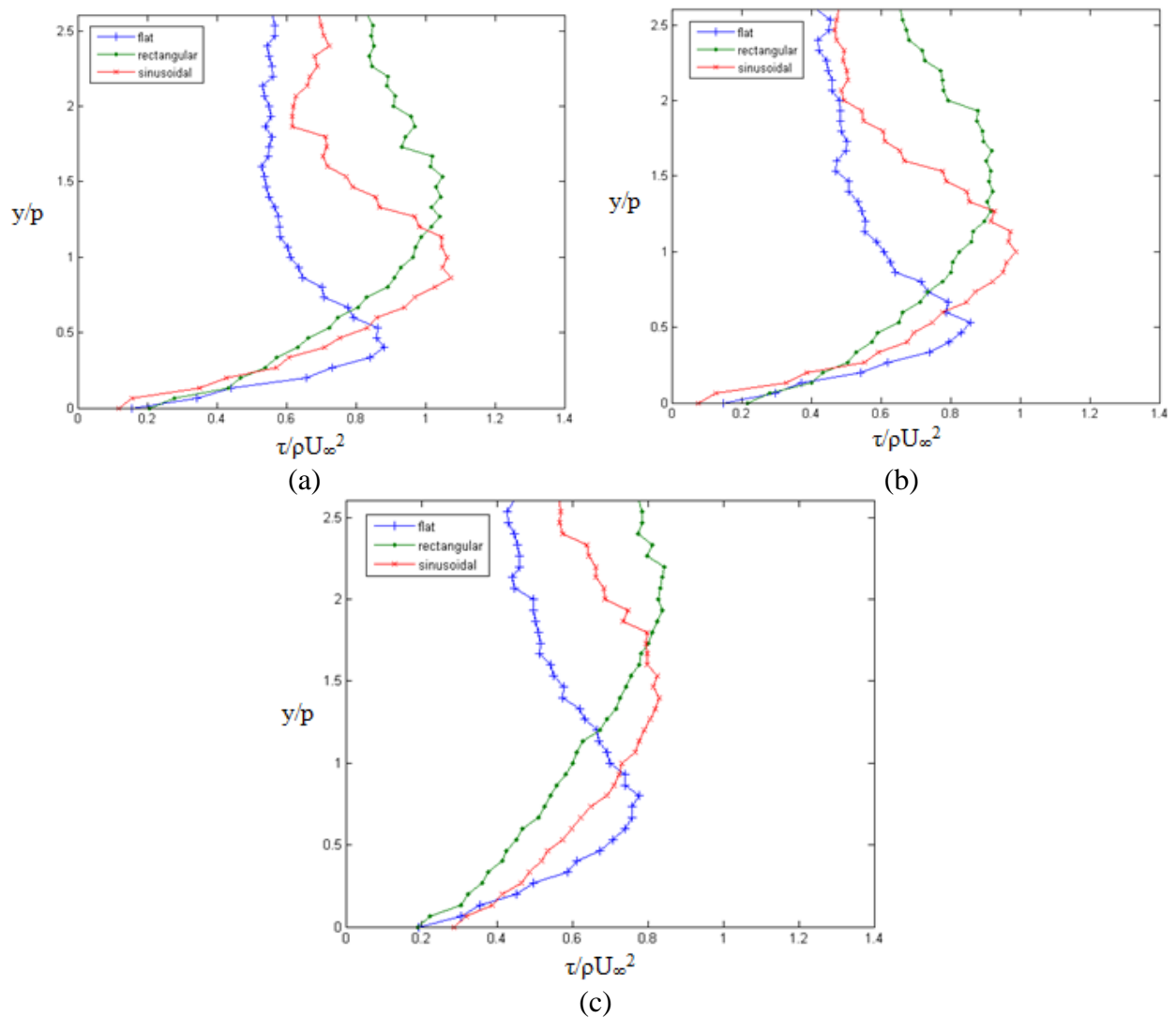


Figure 4.9: Comparison of Reynolds stress profiles for the three plate geometries at the first pressure gradient over groove number (a) 3, (b) 5, and (c) 9

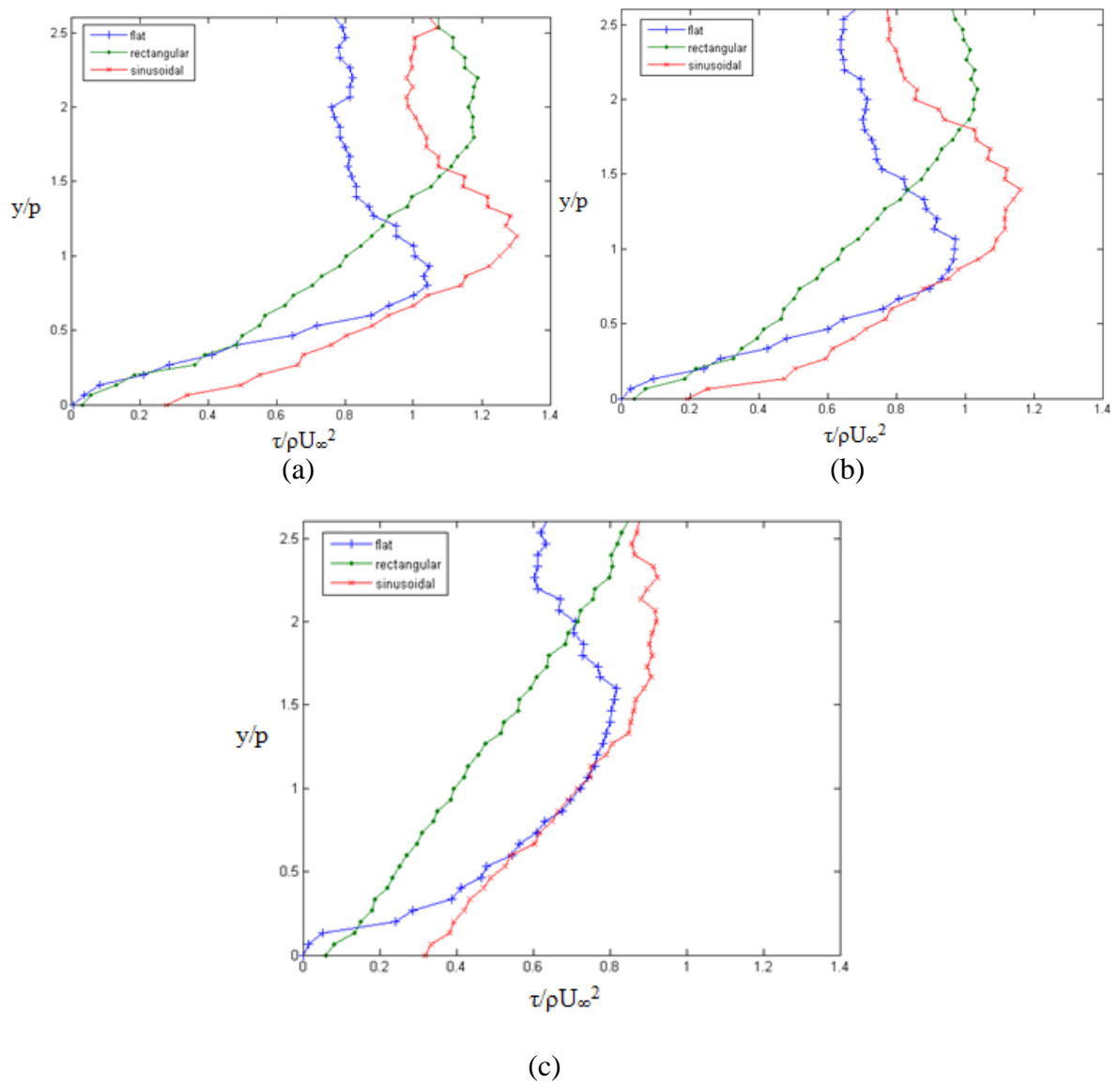


Figure 4.10: Comparison of Reynolds stress profiles for the three plate geometries at the second pressure gradient over groove number (a) 3, (b) 5, and (c) 9

## 4.8 PEAK REYNOLDS STRESS COMPARISON

The value of maximum Reynolds stress is plotted over the length of the investigation region for each of the three plates without a pressure gradient in Figure 4.11.

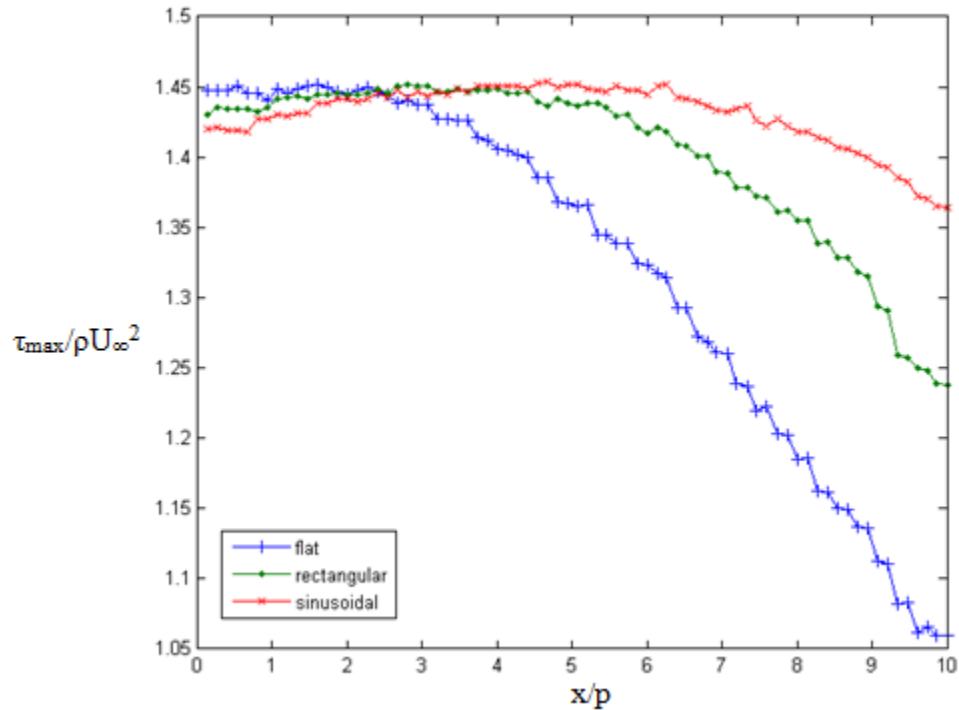
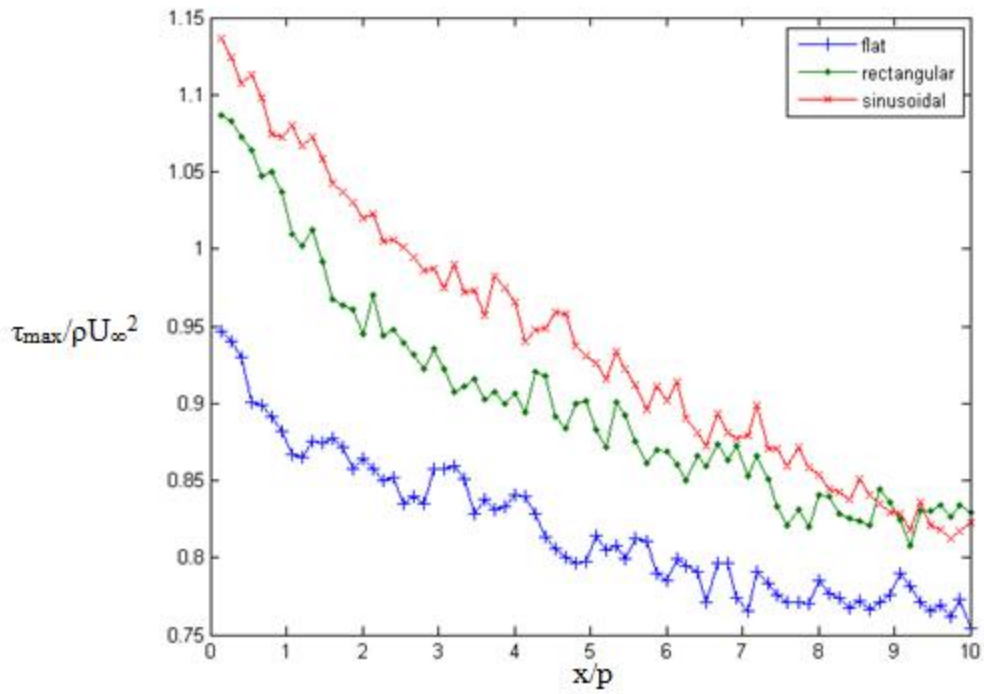


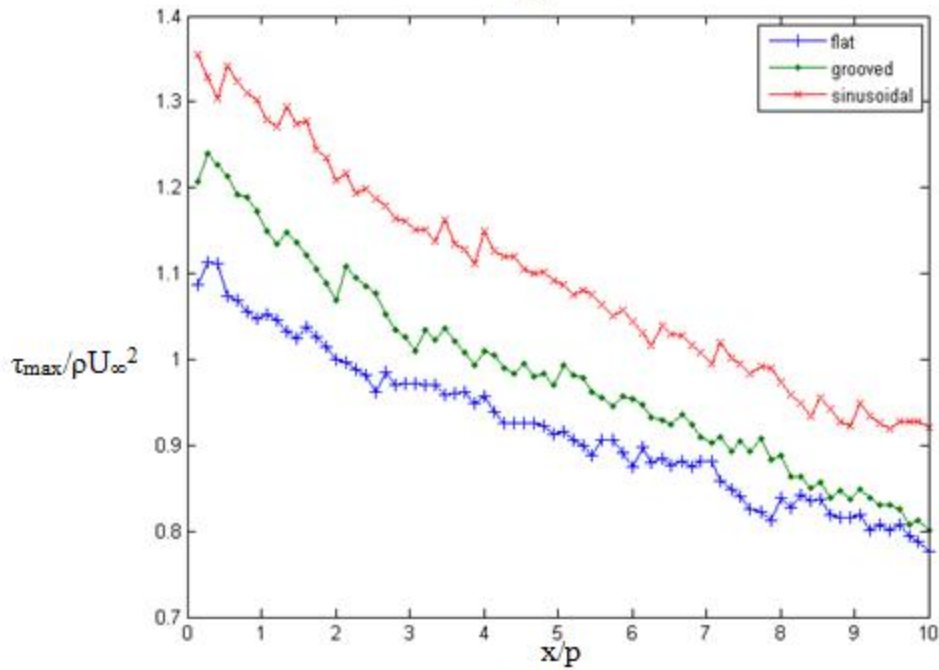
Figure 4.11: Comparison of the values of maximum Reynolds stress over the three plates

It is interesting to note that, toward the beginning to the investigation window, all three surfaces have roughly similar Reynolds stress values. Further downstream, however, the grooved surfaces show greater preservation of Reynolds stress than the flat plate. This conserved momentum near the wall indicates a positive effect of the grooves presence even without the presence of the pressure gradient. The grooves induce mixing even in the zero pressure gradient boundary layer which helps to conserve momentum.

Figure 4.12 shows a comparison of the maximum Reynolds stresses over the three surfaces at the two pressure gradients.



(a)



(b)

Figure 4.12: Comparison of the maximum value of Reynolds stress v. downstream distance over the three surfaces under (a) the first and (b) the second pressure gradient

Figure 4.12 shows that the values of the maximum Reynolds stress over the grooved surfaces are consistently higher than those over the flat surface, with the sinusoids conserving the momentum better than the rectangular grooved surface. This is solid evidence that the sinusoids generate consistently better mixing in the boundary layer than the grooves. Figure 4.13 shows a comparison of the locations of maximum Reynolds stress under the two pressure gradients.

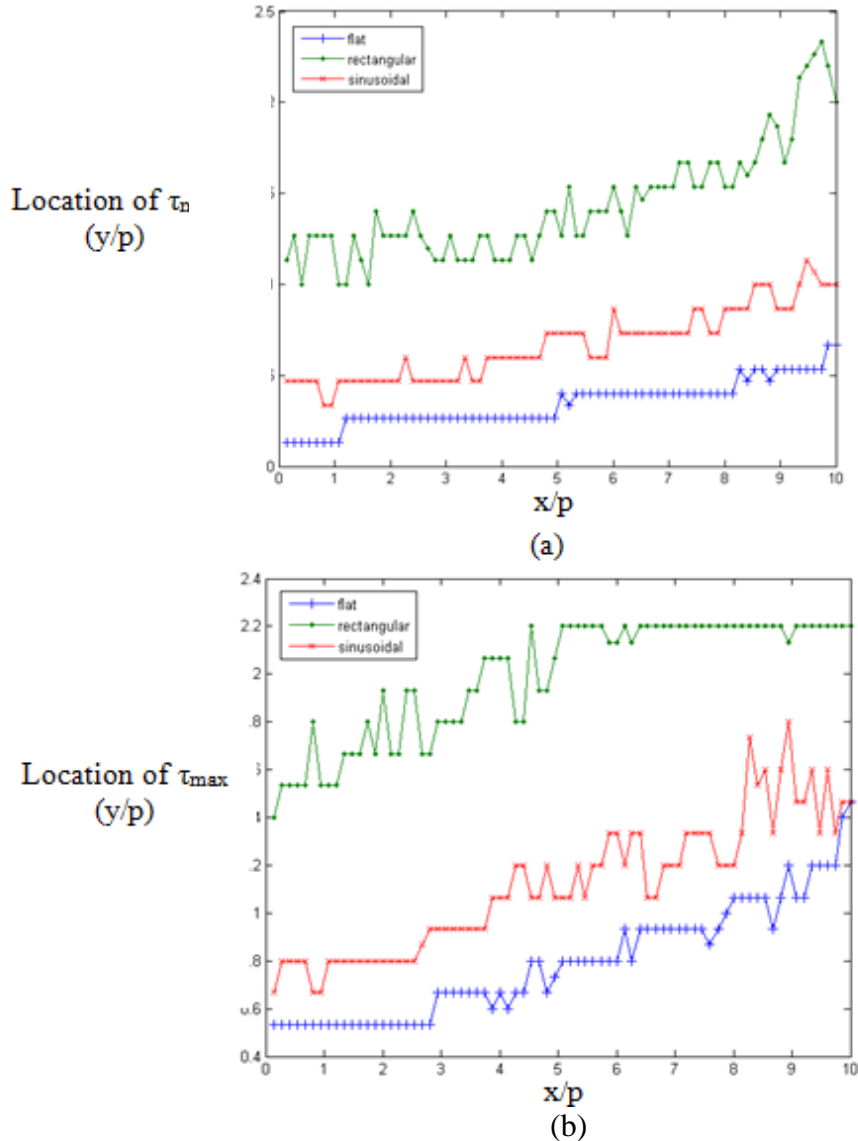


Figure 4.13: Comparison of the height of maximum Reynolds stress over the three surfaces under (a) the first and (b) in second pressure gradient

Figure 4.13 shows that the height of maximum Reynolds stress over the sinusoids is closer to the wall than the maximum value over the rectangular grooves. This indicates better momentum conservation closer to the wall over the sinusoids. This added momentum near the wall signals a more efficient separation control over the sinusoids than the rectangular grooves, indicating that the sinusoids would likely be able to delay separation at pressure gradient strengths beyond the capability of the rectangular grooves. This greater momentum conservation is likely due to better mixing in the near wall region of the boundary layer.

It is important to note that, although the maximum value of Reynolds stress over the flat plate is closer to the wall than the maximum over the sinusoids, the value of Reynolds stress at location of the flat plate maximum is still greater over the sinusoids than the flat plate. Although the location of greatest mixing over the flat plate is closer to the wall than the maximum over the sinusoids, the value of mixing at that location is still greater over the sinusoidal plate.

#### 4.9 MEAN $v$ VELOCITY FIELD COMPARISON

In order to examine possible explanations for this difference in momentum loss between the rectangular grooved and sinusoidal grooved plates,  $v$  velocity contours for both grooved plates under both adverse pressure gradients are compared in Figures 4.11 and 4.12.

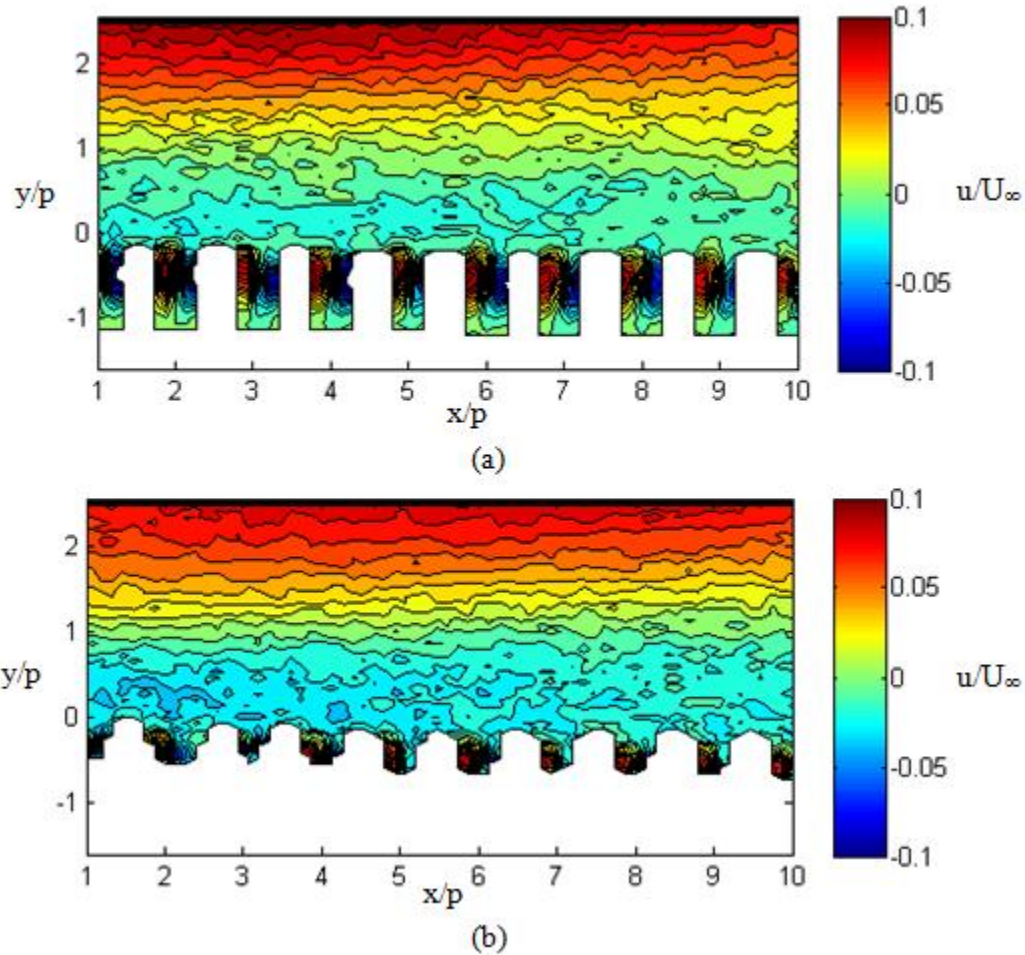


Figure 4.11: Comparison of  $v$  velocity contours over the (a) rectangular and (b) sinusoidal grooved plate at the first pressure gradient

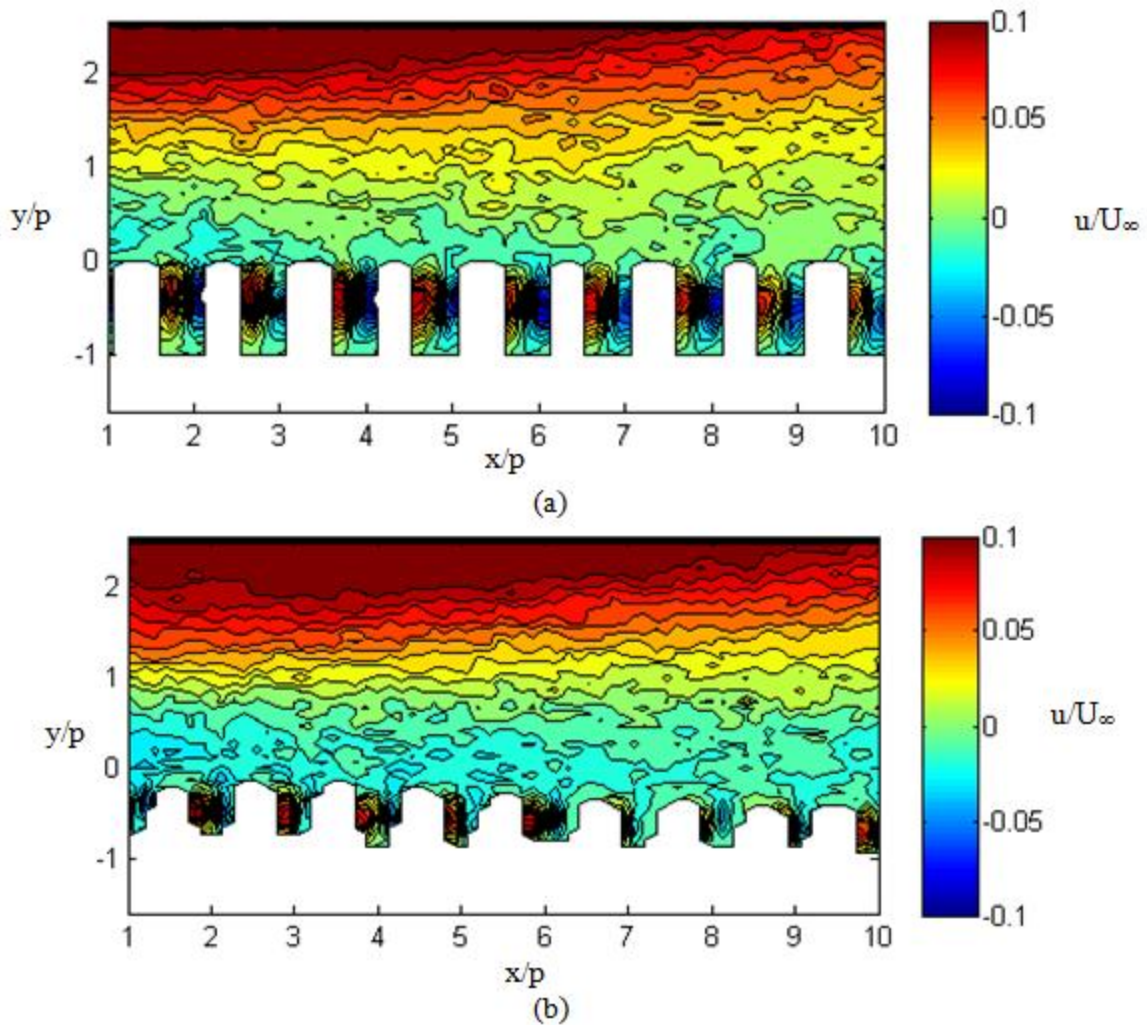
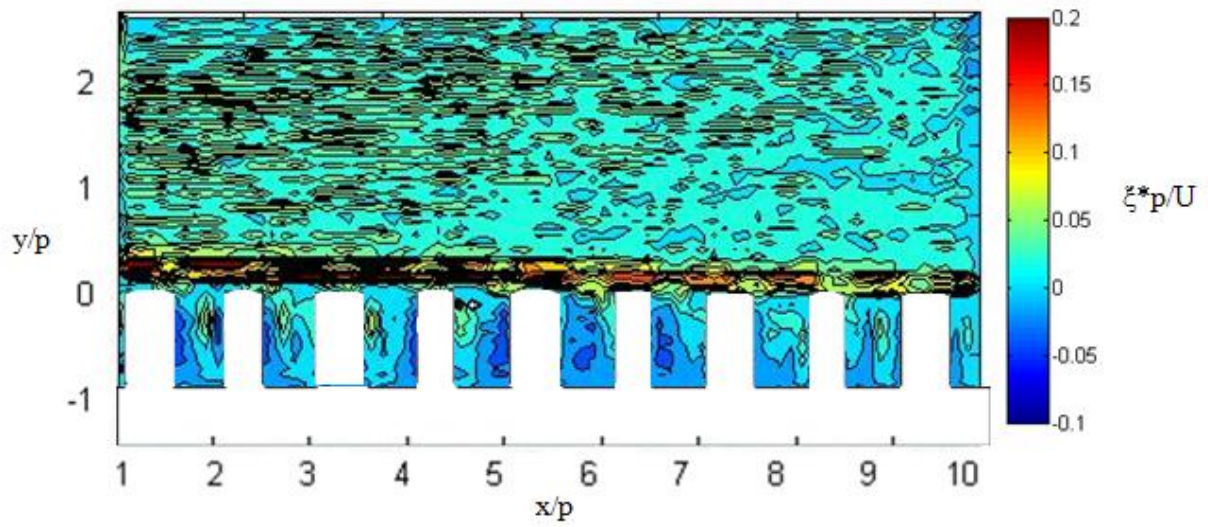


Figure 4.12: Comparison of  $v$  velocity contours over the (a) rectangular and (b) sinusoidal grooved plate at the second pressure gradient

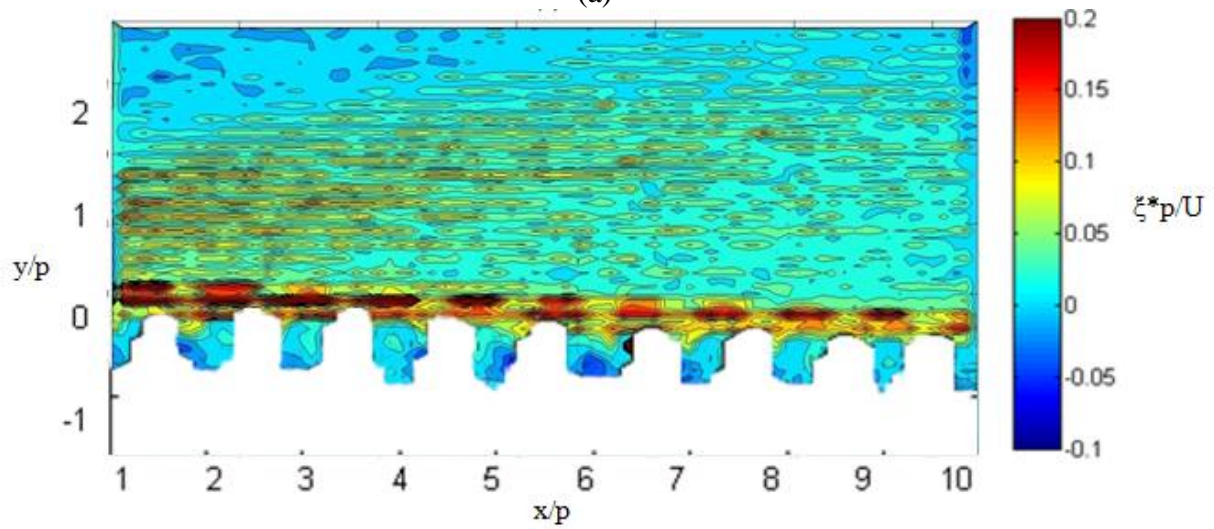
In the rectangular grooved averages, the region of downward moving flow is small occurring just above the cavities as the flow can be seen to be moving into the cavities. The downward components of the imbedded vortices are roughly equal to the upward components. Over the sinusoidal grooves, the region of downward moving flow is larger. The upward component of the imbedded grooves appears to be much larger than the downward component. This indicates more high momentum fluid moving into the near wall region over the sinusoids as compared to the rectangles, resulting in better momentum conservation.

#### 4.10 VORTICITY FIELD COMPARISON

Figure 4.12 shows a comparison of the vorticity fields over the rectangular grooved and sinusoidal grooved surfaces under the second pressure gradient. Appendix A.5 shows the vorticity contours for the first pressure gradient. The vorticity is non-dimensionalized by multiplying by the period of the grooves, and dividing by the free stream velocity. As is expected, all of the vortices embedded with both surfaces rotate in the clockwise direction, producing a negative vorticity. It can be seen in this comparison that the embedded vortices with the sinusoidal grooves are more compact than those embedded inside the rectangular grooves, and reside higher in the groove, closer to the top of the grooves. The vorticity values at the core of the vortices embedded within the sinusoidal grooves are consistently larger than those of the vortices embedded within the rectangular grooves, and the vorticity values with the flow directly above the surface also can be seen to be higher. The differences in the location and strength of the embedded vortices are likely the driving factor in the difference between the two surfaces. A higher rotation rate within the sinusoidal embedded grooves would drive more mixing in the boundary, better conserving the momentum in the near wall region. As is expected, all of the vortices embedded with both surfaces rotate in the clockwise direction, producing a negative vorticity.



(a)



(b)

Figure 4.12: Comparison of vorticity field over the (a) rectangular, and (b) sinusoidal grooved surfaces under the second pressure gradient

#### 4.11 TURBULENCE INTENSITY FIELD COMPARISON

Figure 4.13 shows a comparison of the turbulence intensity contours over the three model surfaces under the first pressure gradient.

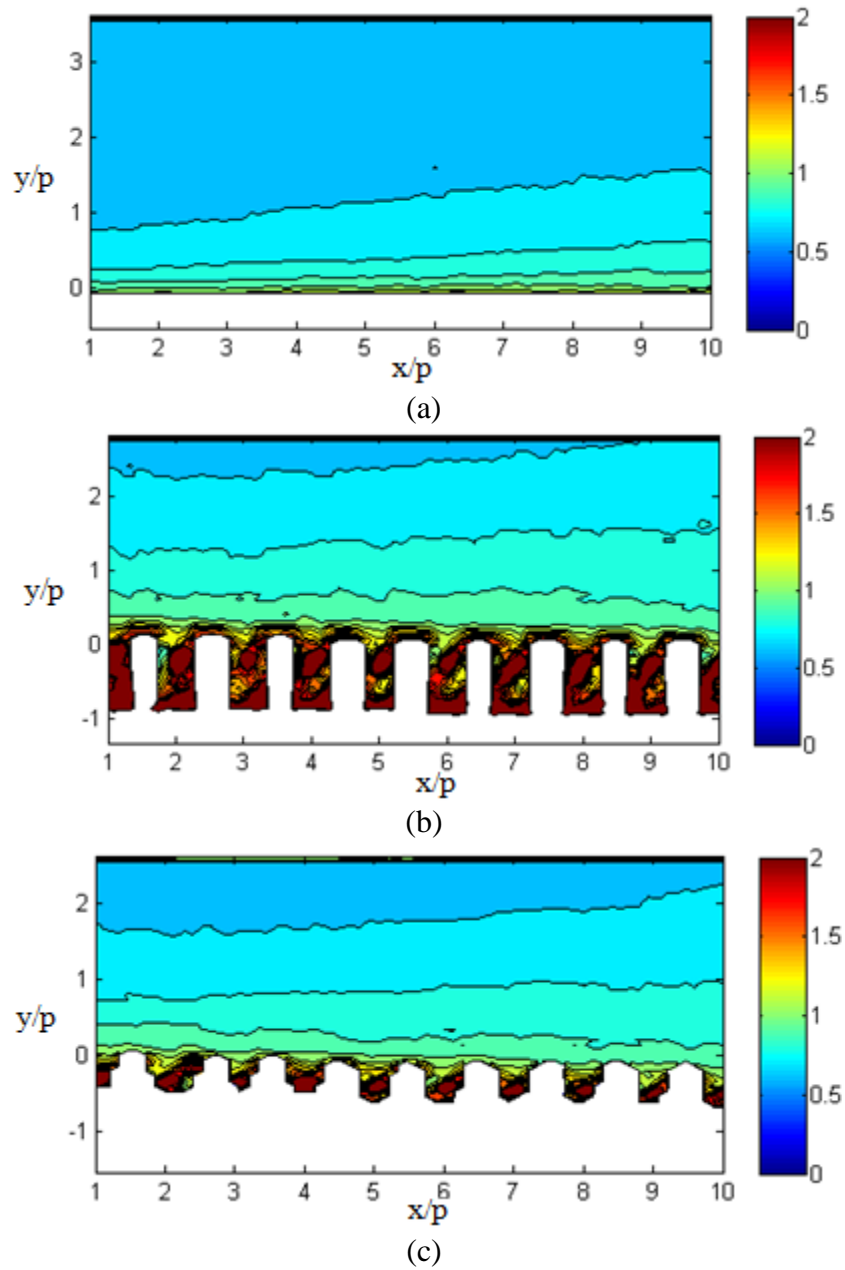


Figure 4.13: Comparison of turbulence intensity field over the (a) flat, (b) rectangular, and (c) sinusoidal plates under the first pressure gradient.

Appendix A.5 shows the turbulence intensity contours for the second pressure gradient. Turbulence intensity is calculated within the grooves even though the cavity Reynolds number of 630 does not indicate turbulent flow would be present. In this context, the turbulence intensity within the grooves is seen indicative of the mixing occurring in the low Reynolds number flow. The contours over the surfaces under the second pressure gradient show similar trends, and are therefore not shown here. As mentioned in the literature, it can be clearly seen that the turbulent fluctuations near the wall in the boundary layer are increased due to the presence of the grooved surfaces. This increase in turbulent fluctuations is indicative of the mixing employed by the grooves to add momentum to the flow near the boundary layer. However, comparing the contours over the rectangular grooved surface to those over the sinusoidal grooved surface reveals similarly shaped and valued contours, indicating that the beneficial added mixing of the sinusoids over the rectangular grooved surface seen thus far cannot be said to be the result of increased turbulence in the flow.

## 5. CONCLUSIONS

### 5.1 MECHANISMS OF BOUNDARY LAYER SEPARATION CONTROL

Under the effect of both pressure gradients induced by the spinning cylinder, flow separation was observed. The backflow coefficient contours showed shallow near wall region of intermittently reversing flow forming an average separation region. These results are consistent with published data regarding the behavior of separating turbulent boundary layers.

Both the rectangular and sinusoidal grooved surfaces were seen to effectively delay boundary layer separation under the effect of the adverse pressure gradient at both strengths. Sustained embedded vortices were seen within the cavities of both surfaces, with the embedded vortices within the sinusoidal surface being located closer to the surface of the groove, having a smaller diameter, and having a stronger vorticity. These embedded vortices created partial slip velocities over the surfaces. The partial slips over the sinusoids were consistently higher than over the rectangular grooves.

Examining the time average velocity profiles over the three model surfaces, the rectangular grooved surface showed a shallower boundary layer profile, while the flat and sinusoidal grooved surfaces showed similar profile characteristics. The Reynolds stress profile comparisons indicated increased fluid mixing near the wall over the grooved plates as compared to the flat plate and particularly higher mixing over the sinusoids as compared to the rectangular grooves. The location of maximum mixing can be seen to be closer to the wall over the sinusoids as

compared to the grooves. This indicates better near wall mixing and increased momentum near the wall. This increased momentum in the near wall region is a likely contributor to the separation control effect, as increased momentum near the wall would oppose the process of separation.

While turbulence intensity contours indicate a roughly equal amount of turbulent fluctuations in the boundary layers over the rectangular and sinusoidal grooved surfaces, the  $v$  velocity average contours show more downward moving flow over the sinusoids. This indicates more high velocity fluid being drawn downward, energizing the near wall fluid. Examining flow within the grooves, the sinusoids show more high speed ejections from the grooves, and fewer injections of high speed fluid, instead drawing in slow moving fluid. Within the rectangular grooves the injections and ejections appear to be roughly equal. This indicates that the rectangular grooves are drawing in high speed fluid, draining that energy from the near wall flow, while the sinusoids draw more low speed fluid, more effectively conserving momentum near the wall.

It can be said that the sinusoidal grooved surface more effectively induces mixing in the boundary layer, adding higher momentum flow near the wall flow while also minimizing the surface drag penalty. As this added momentum appears to be the mechanism for delay in boundary layer separation, the sinusoidal grooves can be said to more effectively delay boundary layer separation than the rectangular grooves. It would be valid to assume that the sinusoids would be able to delay separation at adverse pressure gradients beyond the abilities of the rectangular grooves.

As discussed by Djenidi [5], inflow and outflow of the cavities corresponds with the turbulent structures of high and low speed streaks in the boundary layer. As the low speed streaks are most susceptible to reversal under the effect of the adverse pressure gradient, it is theorized here that the mixing in the near wall boundary layer caused by the grooves weakens these low speed streaks in that the injections of flow into the boundary layer are induced at the location of the low speed streaks. In this way, the cavities are able to delay the onset of boundary layer separation in turbulent boundary layers.

## 5.2 FUTURE WORK

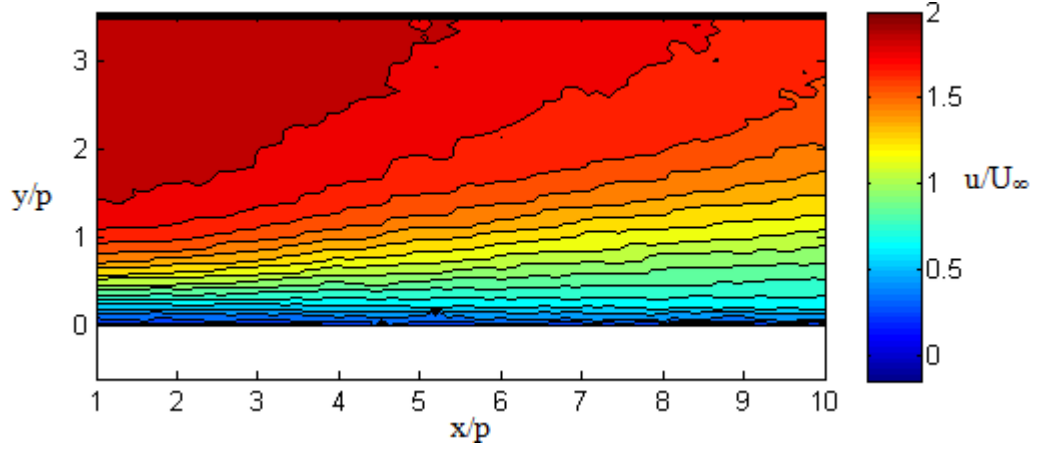
Additional research is needed to investigate the effect of the shape of the grooves on mixing within the boundary layer. Here it has been found that grooves with rounded partitions such as those found on dolphin skin more effectively mix the flow in the boundary layer than rectangular partitions. More research should be done to determine how dependent this mixing is on the width and height of the grooves and the partitions between them. While all data presented here indicates a positive overall effect of the presence of the grooves, future study into the global effect of the embedded vortices on drag over a body is needed. Measurements of drag coefficient over models with and without the presence of the grooves would better indicate an overall positive effect to the presence of the grooves.

## REFERENCES

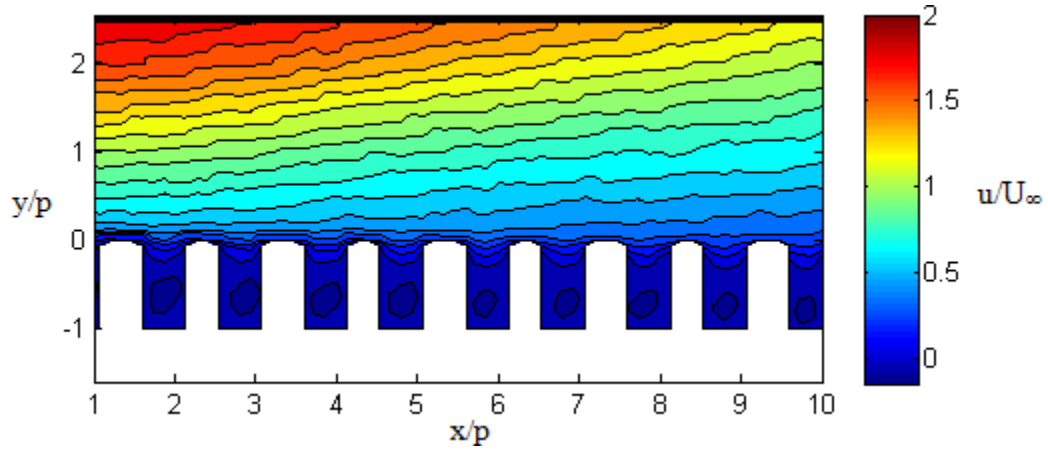
- 1 F. Afroz “Use of a Rotating Cylinder to induce Turbulent Boundary Layer separation on a flat plate,” unpublished.
- 2 K. Angele and B. Muhammad Klingmann, “PIV measurements in a weakly separating and reattaching turbulent boundary layer,” *European Journal of Mechanics BFluids*, vol. 25, no. 2, pp. 204–222, 2006.
- 3 D. W. B. M. Bruse and W. H. R. Meyer, “Fluid Mechanics of Biological Surfaces and their Technological Application,” *Naturwissenschaften*. pp. 157–171, 2000.
- 4 Cassel, “The onset of instability in unsteady boundary layer separation,” *Journal of Fluid Mechanics*, vol. 315, pp. 223–256, 1996.
- 5 L. Djenidi, R. Elavarasan, and R.A. Antonia, “The turbulent boundary layer over transverse square cavities,” *Journal of Fluid Mechanics*, vol. 395, pp. 271-294, 1999.
- 6 F. E. Fish, “The myth and reality of Gray’s paradox: implication of dolphin drag reduction for technology.,” *Bioinspiration biomimetics*, vol. 1, no. 2, pp. R17–R25, Jun. 2006.
- 7 A. W. Lang, “The Shark Skin Effect,” in *Characterization and Technological Applications of Bio-Inspired Surfaces*.
- 8 A. W. Lang, P. Motta, P. Hidalgo, and M. Westcott, “Bristled shark skin: a microgeometry for boundary layer control?,” *Bioinspiration & biomimetics*, vol. 3, no. 4, 2008.
- 9 S. Li, K. Parker, and J. Soria, “A Technique for Generating Adverse Pressure Gradients Using Active and Passive Flow Control Methods,” in *Fourth Australian Conference on Laser Diagnostics in Fluid Mechanics and Combustion.*, University of Adelaide, Australia, 2005, pp 85-88.
- 10 O. Lögdberg, K. Angele, and P. H. Alfredsson, “On the robustness of separation control by streamwise vortices,” *European Journal of Mechanics BFluids*, vol. 29, no. 1, pp. 9–17, 2010.
- 11 J. B. R. Loureiro, a. S. Monteiro, F. T. Pinho, and a. P. Silva Freire, “The effect of roughness on separating flow over two-dimensional hills,” *Experiments in Fluids*, vol. 46, no. 4, pp. 577–596, Dec. 2008.

- 12 V. V Pavlov, "Wing design and morphology of the harbor porpoise dorsal fin.," *Journal of Morphology*, vol. 258, no. 3, pp. 284–295, 2003.
- 13 S. B. Pope, "Wall flows," in *Turbulent Flows*, Cambridge, UK: Cambridge University Press, 2000, ch. 7, sec. 7.3, pp. 299-327.
- 14 G. V Selby, J. C. Lin, and F. G. Howard, "Turbulent Flow Separation Control Over a Backward-Facing Ramp Via Transverse and Swept Grooves," *Journal of Fluids Engineering*, vol. 112, no. June, pp. 238–240, 1990.
- 15 Simpson, R.L. 1997. Aspects of Turbulent Boundary-Layer Separation. *Prog Aerospace Sci.* vol. 32, pp. 457-521, 1996
- 16 S. H. Ridgway and D. a Carder, "Features of dolphin skin with potential hydrodynamic importance," *IEEE Engineering in Medicine and Biology Magazine*, vol. 12, no. 3, pp. 83–88, 1993.
- 17 F. G. Howard and W. L. Goodman, "Axisymmetric Bluff-Body Drag Reduction Through Geometrical Modification," *Journal of Aircraft*, vol. 22, no. 61, pp. 516–522, 1985.
- 18 Willert, C.E. & Gharib, 1991. Digital Image Particle Velocimetry. *Experiments in Fluids* vol. 10, pp. 181-193.

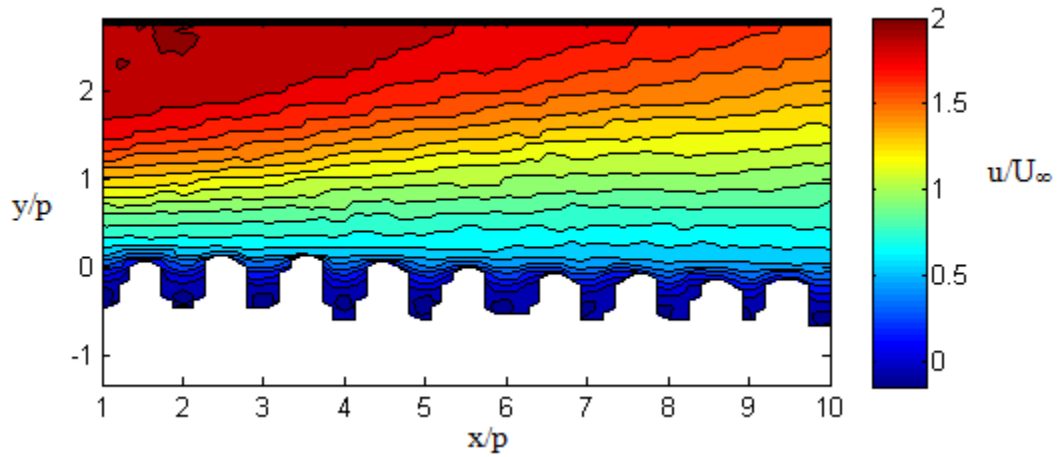
APPENDIX A – ADDITIONAL DATA



(a)

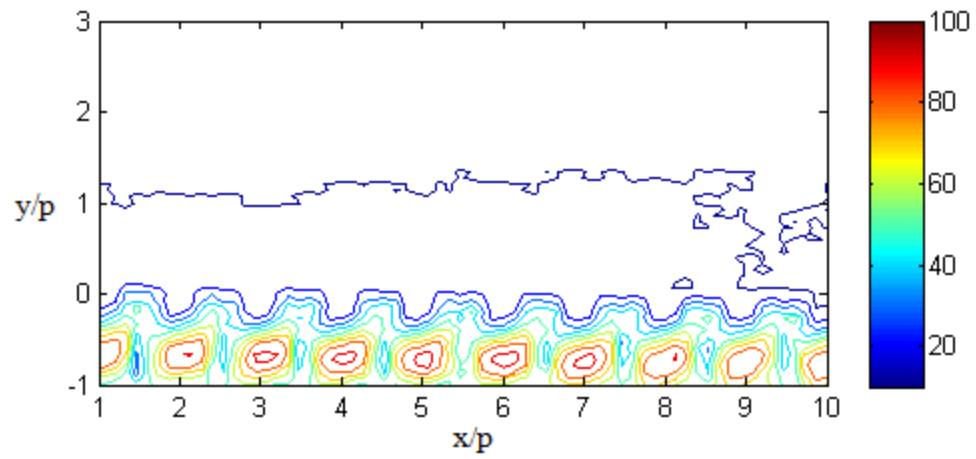


(b)

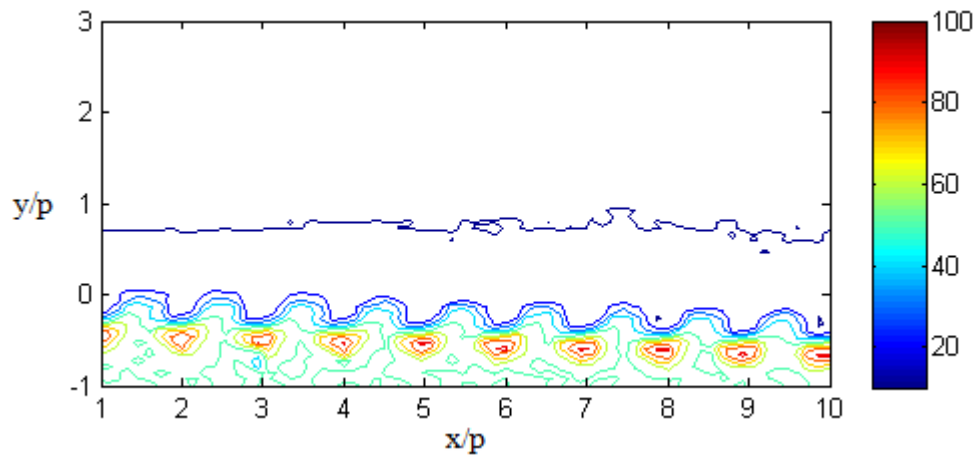


(c)

A.1: Average U velocity contours over the (a) flat, (b) rectangular, and (c) sinusoidal surfaces under the second pressure gradient

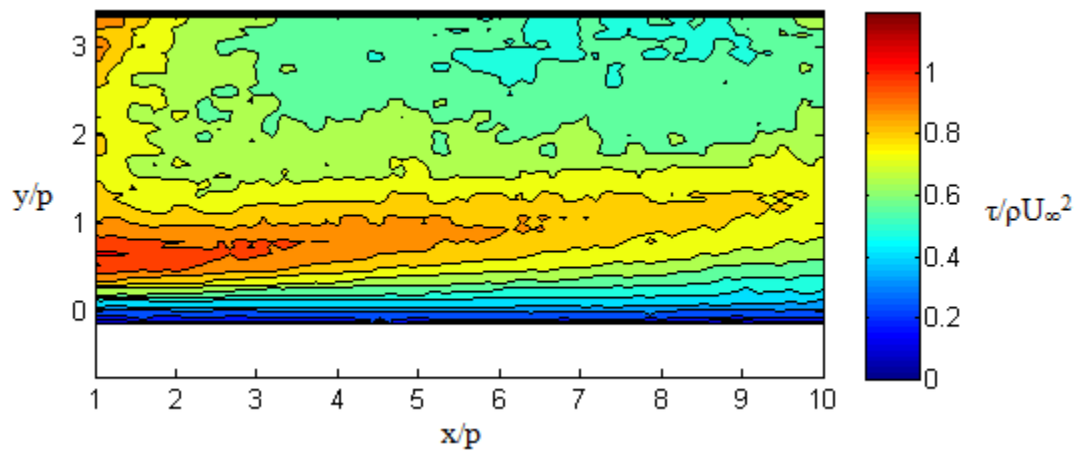


(a)

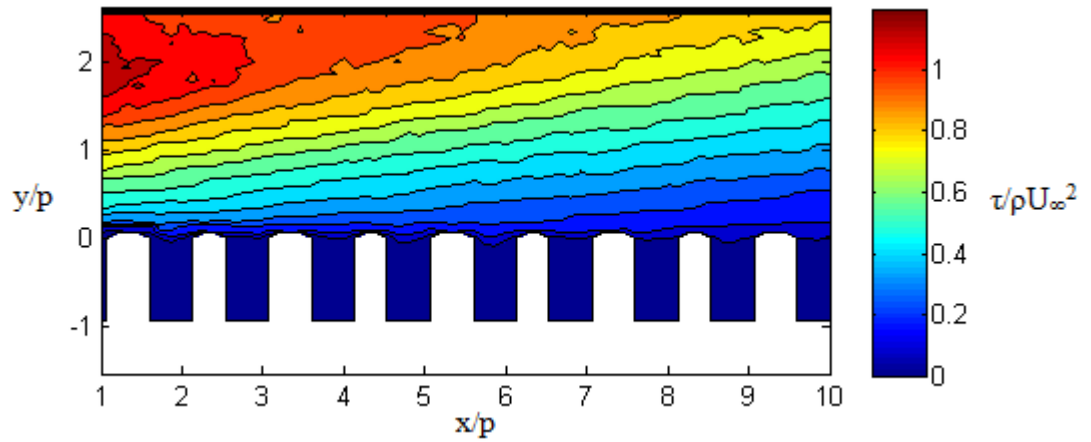


(b)

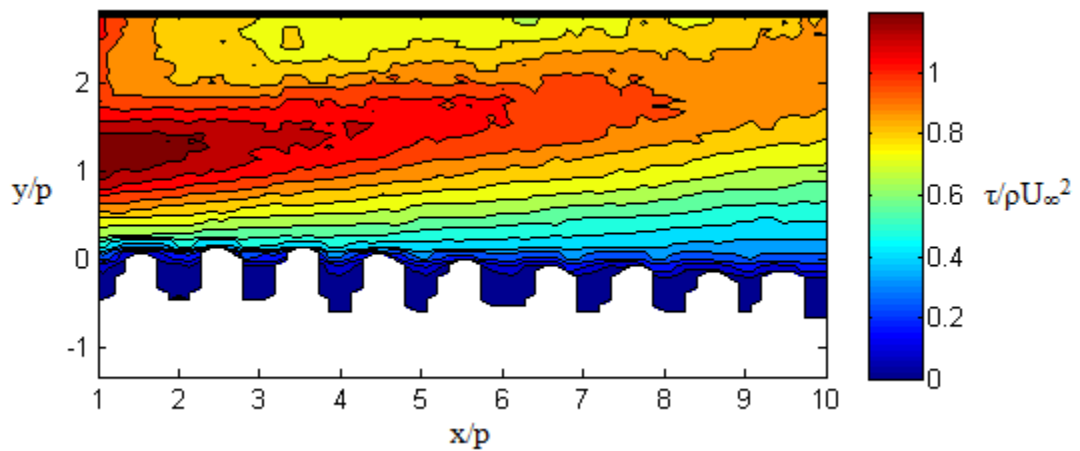
A.2: Backflow coefficient contours over (a) the rectangular and (b) in sinusoidal surfaces under the 1<sup>st</sup> pressure gradient



(a)

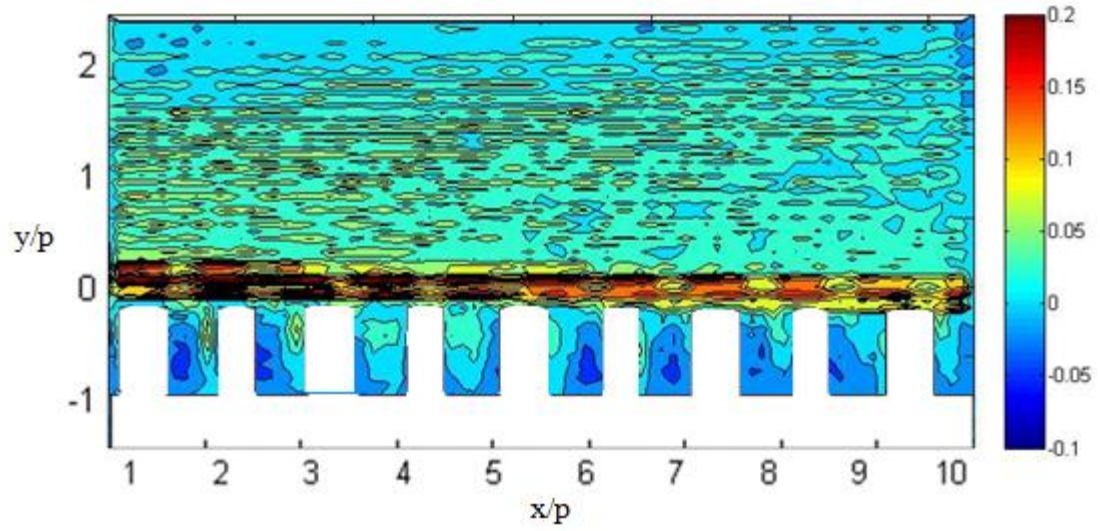


(b)

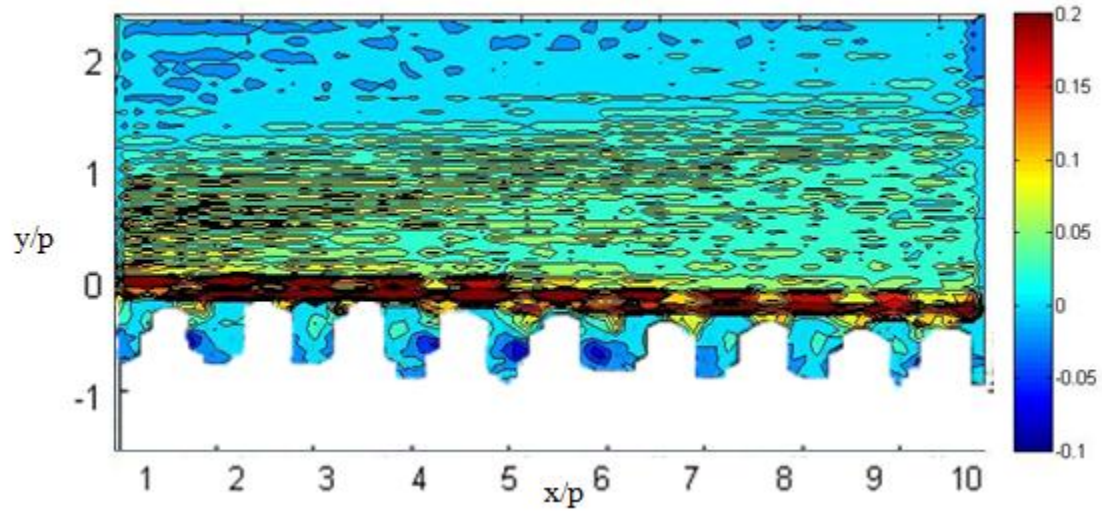


(c)

A.3: Reynolds stress contours over (a) the flat, (b) the rectangular, and (c) the sinusoidal surfaces under the 2<sup>nd</sup> pressure gradient

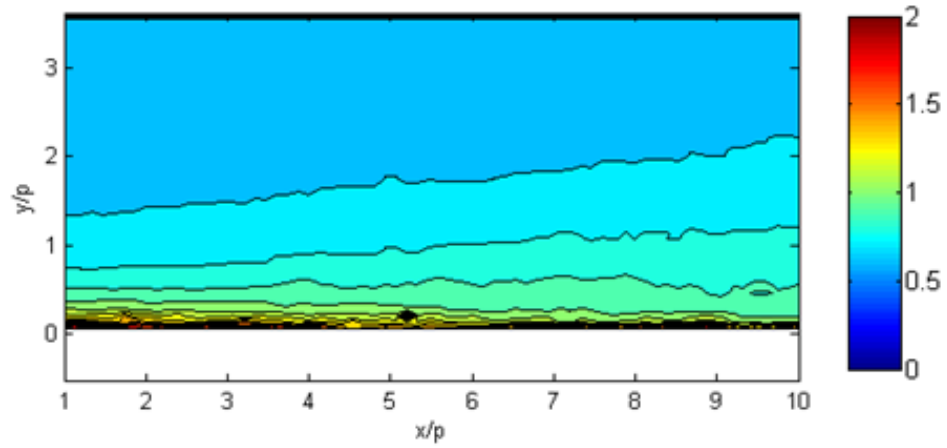


(a)

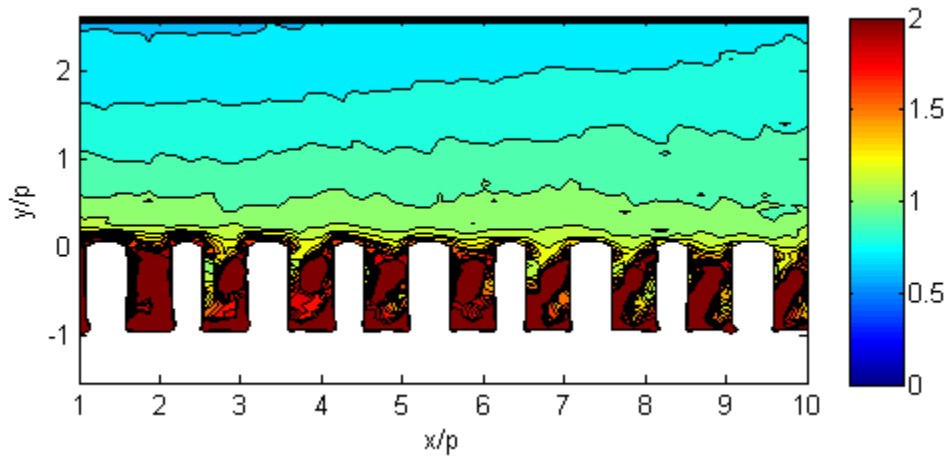


(b)

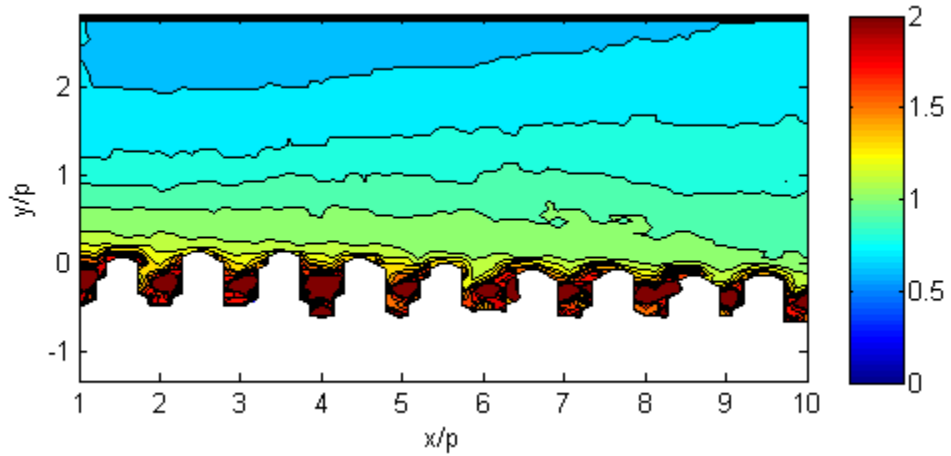
A.4: Vorticity contours over (a) the rectangular and (b) in sinusoidal surfaces under the 1<sup>st</sup> pressure gradient



(a)



(b)



(c)

A.5: Turbulence intensity contours over (a) the flat, (b) the rectangular, and (c) the sinusoidal surfaces under the 2<sup>nd</sup> pressure gradient

## APPENDIX B – UNCERTAINTY ANALYSIS

Several sources of error exist in digital particle image velocimetry that should be mentioned. The accepted value of error in the calculation of the displacement of a particle during PIV processing is 1% [18]. The length calibration for these data sets was calculated by placing a ruler within the plane of the laser sheet and taking an image. The pixel to distance ratio was then calculated manually by counting the pixels between two centimeter markers on the ruler. For this data, the calibration was calculated to be 25 micrometers per pixel. Due to the thickness of the centimeter markers on the ruler, and any potential tilt in the ruler in the image, this calculation is a potential source of error. Assuming an error of within 5 pixels, the error in the length scale would be 2.5%. Because the camera remained stationary for all sets of data, and the same calibration was used in every processing set, this error would be a consistent offset throughout the data. The edge of the surface often occurs in the middle of a processing grid. These grids being 16 pixels in height, error in the calculation of the edge of the surface may be as high as .2 millimeters, or 1.67% of the total height of image. Combining these sources of error, the maximum error in any calculated velocity vector is 3.16%.

An additional source of error in the velocity vector calculation lies in the method employed to determine the average velocity vector for each point in the investigation window. For every image processed, the processing software calculates the vector and then determines whether or not the calculated value of that vector is accurate by checking the vectors around it. If the vector isn't deemed valid, the software tags it thus, and the value of that vector is not added

with the others to determine the average. However, the calculation of the average assumes 10,000 good vectors and divides by that number. The PIV processing software gives an average percentage of valid vectors in each processing window, and smallest value given for the data examined here was 94% good vectors. The error introduced to the average by the inaccurate total number of vectors for this percentage of good vectors is 6%. Areas of bad seeding and particles moving in and out of the plane of the laser sheet are the primary causes of these bad vectors. Efforts to minimize three-dimensional flow and insure proper seeding could be employed to reduce this error.